

The abundance and excitation of molecular anions in interstellar clouds[★]

M. Agúndez¹, N. Marcelino^{2,3}, B. Tercero^{2,3}, I. Jiménez-Serra⁴, and J. Cernicharo¹

¹ Instituto de Física Fundamental, CSIC, Calle Serrano 123, E-28006 Madrid, Spain
e-mail: marcelino.agundez@csic.es

² Observatorio Astronómico Nacional, IGN, Calle Alfonso XII 3, E-28014 Madrid, Spain

³ Observatorio de Yebes, IGN, Cerro de la Palera s/n, E-19141 Yebes, Guadalajara, Spain

⁴ Centro de Astrobiología (CSIC/INTA), Ctra. de Torrejón a Ajalvir km 4, 28806, Torrejón de Ardoz, Spain

Received; accepted

ABSTRACT

We report new observations of molecular anions with the Yebes 40m and IRAM 30m telescopes toward the cold dense clouds TMC-1 CP, Lupus-1A, L1527, L483, L1495B, and L1544. We detected for the first time C_3N^- and C_5N^- in Lupus-1A and C_4H^- and C_6H^- in L483. In addition, we report new lines of C_6H^- toward the six targeted sources, of C_4H^- toward TMC-1 CP, Lupus-1A, and L1527, and of C_8H^- and C_3N^- in TMC-1 CP. Excitation calculations using recently computed collision rate coefficients indicate that the lines of anions accessible to radiotelescopes run from subthermally excited to thermalized as the size of the anion increases, with the degree of departure from thermalization depending on the H_2 volume density and the line frequency. We noticed that the collision rate coefficients available for the radical C_6H cannot explain various observational facts, which advises for a revisitation of the collision data for this species. The observations presented here, together with observational data from the literature, are used to model the excitation of interstellar anions and to constrain their abundances. In general, the anion-to-neutral ratios derived here agree within 50% (a factor of two at most) with literature values, when available, except for the C_4H^-/C_4H ratio, which shows higher differences due to a revision of the dipole moment of C_4H . From the set of anion-to-neutral abundance ratios derived two conclusions can be drawn. First, the C_6H^-/C_6H ratio shows a tentative trend in which it increases with increasing H_2 density, as expected from theoretical grounds. And second, it is incontestable that the higher the molecular size the higher the anion-to-neutral ratio, which supports a formation mechanism based on radiative electron attachment. Nonetheless, calculated rate coefficients for electron attachment to the medium size species C_4H and C_3N are probably too high and too low, respectively, by more than one order of magnitude.

Key words. astrochemistry – line: identification – molecular processes – radiative transfer – ISM: molecules – radio lines: ISM

1. Introduction

The discovery of negatively charged molecular ions in space has been a relatively recent finding (McCarthy et al. 2006). To date the inventory of molecular anions detected in interstellar and circumstellar clouds consists of four hydrocarbon anions, C_4H^- (Cernicharo et al. 2007), C_6H^- (McCarthy et al. 2006), C_8H^- (Brünken et al. 2007a; Remijan et al. 2007), and $C_{10}H^-$ (Remijan et al. 2023), and four nitrile anions, CN^- (Agúndez et al. 2010), C_3N^- (Thaddeus et al. 2008), C_5N^- (Cernicharo et al. 2008), and C_7N^- (Cernicharo et al. 2023a). The astronomical detection of most of these species has been possible thanks to the laboratory characterization of their rotational spectrum (McCarthy et al. 2006; Gupta et al. 2007; Gottlieb et al. 2007; Thaddeus et al. 2008). However, the astronomical detection of C_5N^- , C_7N^- , and $C_{10}H^-$ is based on high level *ab initio* calculations and astrochemical arguments (Botschwina & Oswald 2008; Cernicharo et al. 2008, 2020, 2023a; Remijan et al. 2023). In fact, in the case of

$C_{10}H^-$ it is not yet clear whether the identified species is $C_{10}H^-$ or C_9N^- (Pardo et al. 2023).

The current situation is such that there is only one astronomical source where the eight molecular anions have been observed, the carbon-rich circumstellar envelope IRC +10216 (McCarthy et al. 2006; Cernicharo et al. 2007, 2008; Remijan et al. 2007; Thaddeus et al. 2008; Agúndez et al. 2010; Cernicharo et al. 2023a; Pardo et al. 2023), while the first negative ion discovered, C_6H^- (McCarthy et al. 2006), continues to be the most widely observed in astronomical sources (Sakai et al. 2007, 2010; Gupta et al. 2009; Cordiner et al. 2011, 2013).

Observations indicate that along each of the series $C_{2n+2}H^-$ and $C_{2n-1}N^-$ (with $n = 1, 2, 3, 4$) the anion-to-neutral abundance ratio increases with increasing molecular size (Millar et al. 2017). This is expected according to the formation mechanism originally proposed by Herbst (1981), which involves the radiative electron attachment to the neutral counterpart of the anion (Herbst & Osamura 2008; Carelli et al. 2013). However, the efficiency of this mechanism in interstellar space has been disputed (Khamesian et al. 2016), and alternative formation mechanisms have been proposed (Gianturco et al. 2016). Currently there is not yet consensus on the formation mechanism of molecular anions in space (see discussion in Millar et al. 2017). Moreover, detections of negative ions other than C_6H^- in interstellar clouds

[★] Based on observations carried out with the Yebes 40m telescope (projects 19A003, 20A014, 20A016, 20B010, 20D023, 21A006, 21A011, 21D005, 22B023, and 23A024) and the IRAM 30m telescope. The 40m radio telescope at Yebes Observatory is operated by the Spanish Geographic Institute (IGN; Ministerio de Transportes, Movilidad y Agenda Urbana). IRAM is supported by INSU/CNRS (France), MPG (Germany), and IGN (Spain).

are scarce, and thus our view of the abundance of the different anions in interstellar space is statistically very limited.

Apart from the anion-to-anion behavior it is also interesting to know which is the source-to-source behavior. That is, how does the abundance of anions behave from one source to another. Based on C_6H^- detections, the C_6H^-/C_6H abundance ratio seems to increase with increasing H_2 volume density (Sakai et al. 2007; Agúndez et al. 2008; Cordiner et al. 2013), which is expected from chemical considerations (e.g., Flower et al. 2007; see also Sect. 6). However, most anion detections in interstellar clouds have been based on one or two lines and their abundances have been estimated assuming that their rotational levels are populated according to local thermodynamic equilibrium (LTE), which may not be a good assumption given the large dipole moments, and thus high critical densities, of anions. Recently, rate coefficients for inelastic collisions with H_2 or He have been calculated for C_2H^- (Dumouchel et al. 2012; Gianturco et al. 2019; Franz et al. 2020; Toumi et al. 2021; Dumouchel et al. 2023), C_4H^- (Senent et al. 2019; Balança et al. 2021), C_6H^- (Walker et al. 2016, 2017), CN^- (Kłos & Lique 2011; González-Sánchez et al. 2020), C_3N^- (Lara-Moreno et al. 2017, 2019; Tchakoua et al. 2018), and C_5N^- (Biswas et al. 2023), which makes it possible to study the excitation of anions in the interstellar medium.

Here we report new detections of anions in interstellar sources. Concretely, we detected C_3N^- and C_5N^- in Lupus-1A and C_6H^- and C_4H^- in L483. We also present the detection of new lines of C_4H^- , C_6H^- , C_8H^- , C_3N^- , and C_5N^- in interstellar clouds where these anions have been already observed. We use the large observational dataset from this study, together with that available from the literature, to review the observational status of anions in interstellar clouds and to carry out a comprehensive analysis of the abundance and excitation of anions in the interstellar medium.

2. Observations

2.1. Yebes 40m and IRAM 30m observations from this study

The observations of cold dark clouds presented in this study were carried out with the Yebes 40m and IRAM 30m telescopes. We targeted the starless core TMC-1 at the cyanopolyne peak position (hereafter TMC-1 CP)¹, the starless core Lupus-1A², the prestellar cores L1495B³ and L1544⁴, and the dense cores L1527⁵ and L483⁶, which host a Class 0 protostar. All observations were done using the frequency switching technique to maximize the on-source telescope time and to improve the sensitivity of the spectra.

The Yebes 40m observations consisted in a full scan of the Q band (31-50 GHz) acquired in a single spectral setup with a 7 mm receiver, which was connected to a fast Fourier transform spectrometer that provides a spectral resolution of 38 kHz (Tercero et al. 2021). The data of TMC-1 CP are part of the on-going QUIJOTE line survey (Cernicharo et al. 2021). The spectra used here were obtained between November 2019 and November 2022 and contain a total of 758 h of on-source telescope time in each polarization (twice this value after averaging both polarizations). Two frequency throws of 8 and 10 MHz

were used. The sensitivity ranges from 0.13 to 0.4 mK in antenna temperature. The data of L1544 were taken between October and December 2020 toward the position of the methanol peak of this core, where complex organic molecules have been detected (Jiménez-Serra et al. 2016), and are part of a high-sensitivity Q-band survey (31 h on-source; Jiménez-Serra et al. in prep.). The data for the other sources were obtained from July 2020 to February 2023 for L483 (the total on-source telescope time is 103 h), from May to November 2021 for L1527 (40 h on-source), from July 2021 to January 2023 for Lupus-1A (120 h on-source), and from September to November 2021 for L1495B (45 h on-source). Different frequency throws were adopted depending on the observing period, which resulted from tests done at the Yebes 40m telescope to find the optimal frequency throw. We used frequency throws of 10 MHz and 10.52 MHz for L483, 10 MHz for L1544, 8 MHz for L1527, and 10.52 MHz for Lupus-1A and L1495B. The antenna temperature noise levels, after averaging horizontal and vertical polarizations, are in the range 0.4-1.0 mK for L483, 1.3-1.8 mK for L1544, 0.7-2.7 mK for L1527, 0.7-2.8 mK for Lupus-1A, and 0.8-2.6 mK for L1495B.

The observations carried out with the IRAM 30m telescope used the 3 mm EMIR receiver connected to a fast Fourier transform spectrometer that provides a spectral resolution of 49 kHz. Different spectral regions within the 3 mm band (72-116 GHz) were covered depending on the source. The data of TMC-1 CP consist of a 3 mm line survey (Marcelino et al. 2007; Cernicharo et al. 2012) and spectra observed in 2021 (Agúndez et al. 2022; Cabezas et al. 2022). The data of L483 consists of a line survey in the 80-116 GHz region (see Agúndez et al. 2019), together with data in the 72-80 GHz region, which are described in Cabezas et al. (2021). Data of Lupus-1A, L1495B, L1521F, L1251A, L1512, L1172, and L1389 were observed from September to November 2014 during a previous search for molecular anions at mm wavelengths (see Agúndez et al. 2015). Additional data of Lupus-1A were gathered during 2021 and 2022 during a project aimed to observe H_2NC (Agúndez et al. 2023). In the case of L1527, the IRAM 30m data used were observed in July and August 2007 with the old ABCD receivers connected to an autocorrelator that provided spectral resolutions of 40 or 80 kHz (Agúndez et al. 2008).

The half power beam width (HPBW) of the Yebes 40m telescope is in the range 35-57'' in the Q band, while that of the IRAM 30m telescope ranges between 21'' and 34'' in the 3 mm band. The beam size can be fitted as a function of frequency as $HPBW('') = 1763/\nu(\text{GHz})$ for the Yebes 40m telescope and as $HPBW('') = 2460/\nu(\text{GHz})$ for the IRAM 30m telescope. Therefore, the beam size of the IRAM 30m telescope at 72 GHz is similar to that of the Yebes 40m at 50 GHz. The intensity scale in both the Yebes 40m and IRAM 30m telescopes is antenna temperature, T_A^* , for which we estimate a calibration error of 10%. To convert antenna temperature into main beam brightness temperature see foot of Table A.1. All data were analyzed using the program CLASS of the GILDAS software⁷.

2.2. Observational dataset of anions in dark clouds

In Table A.1 we compile the line parameters of all the lines of negative molecular ions detected toward cold dark clouds, including lines from this study and from the literature. The line parameters of C_7N^- observed toward TMC-1 CP are given in Cernicharo et al. (2023a) and are not repeated here. In the case

⁷ <https://www.iram.fr/IRAMFR/GILDAS/>

¹ TMC-1 CP: $\alpha_{J2000} = 4^h 41^m 41.9^s$ and $\delta_{J2000} = +25^\circ 41' 27.0''$

² Lupus-1A: $\alpha_{J2000} = 15^h 42^m 52.4^s$ and $\delta_{J2000} = -34^\circ 07' 53.5''$

³ L1495B: $\alpha_{J2000} = 4^h 15^m 41.8^s$ and $\delta_{J2000} = +28^\circ 47' 46.0''$

⁴ L1544: $\alpha_{J2000} = 5^h 4^m 18.0^s$ and $\delta_{J2000} = +25^\circ 11' 10.0''$

⁵ L1527: $\alpha_{J2000} = 4^h 39^m 53.9^s$ and $\delta_{J2000} = +26^\circ 03' 11.0''$

⁶ L483: $\alpha_{J2000} = 18^h 17^m 29.8^s$ and $\delta_{J2000} = -4^\circ 39' 38.3''$

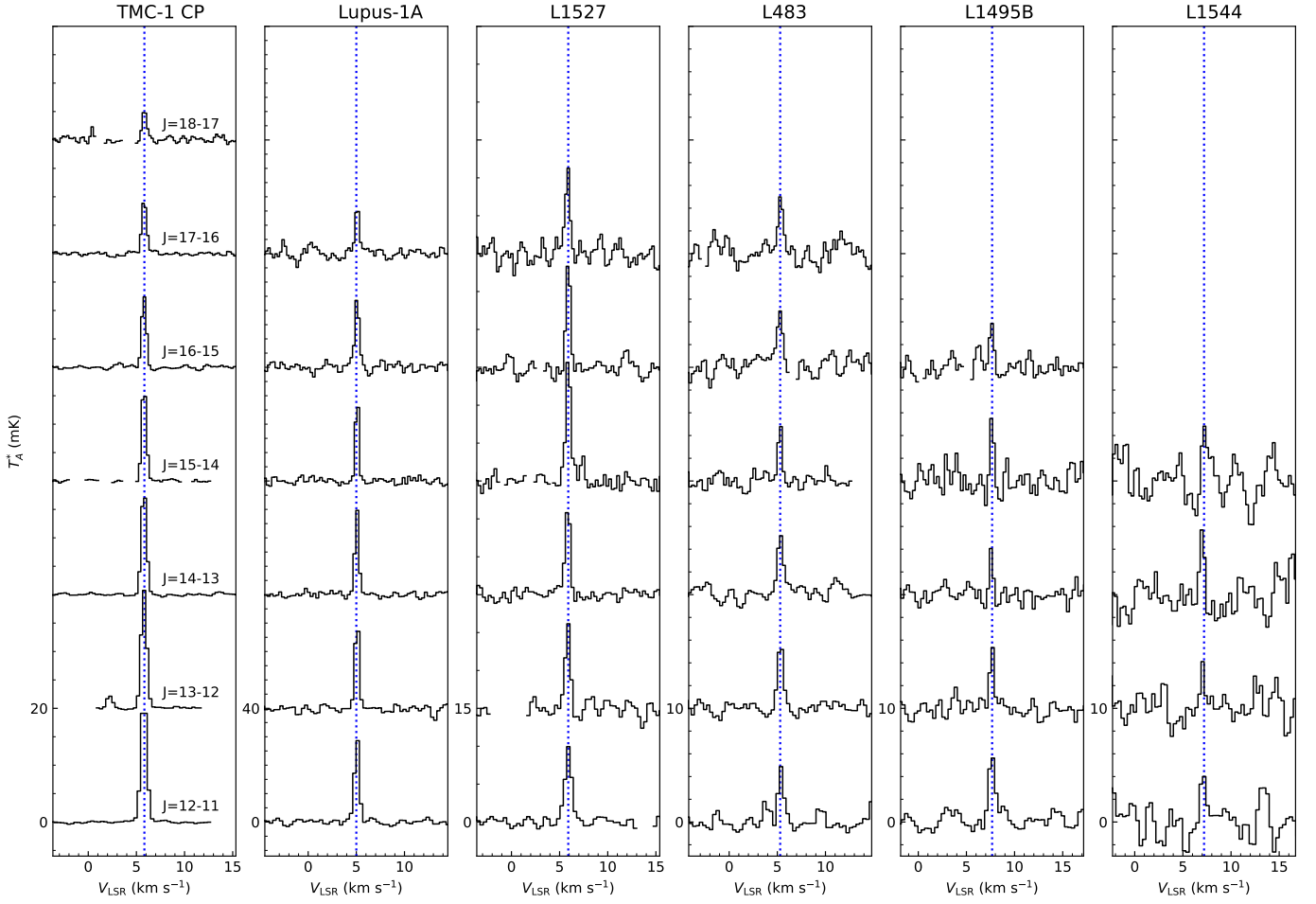


Fig. 1. Lines of C_6H^- observed in this work toward six cold dense clouds using the Yebes 40m telescope. See line parameters in Table A.1.

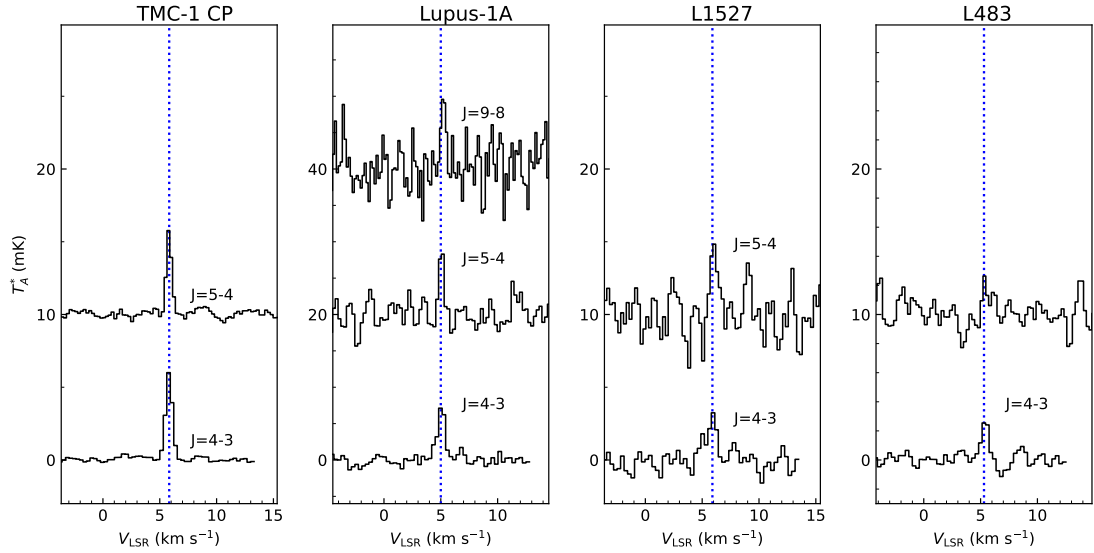


Fig. 2. Lines of C_4H^- observed in this work toward TMC-1 CP, Lupus-1A, L1527, and L483 using the Yebes 40m and IRAM 30m telescopes. See line parameters in Table A.1.

of $C_{10}H^-$ in TMC-1 CP we do not include line parameters here because the detection by Remijan et al. (2023) is not based on individual lines but on spectral stack of many lines. The lines of molecular anions presented in this study are shown in Fig. 1 for C_6H^- , Fig. 2 for C_4H^- , and Fig. 3 for the remaining anions, i.e.,

C_8H^- , C_3N^- , and C_5N^- . Since we are interested in the determination of anion-to-neutral abundance ratios, we also need the lines of the corresponding neutral counterpart of each molecular anion, which are the radicals C_4H , C_6H , C_8H , C_3N , and C_5N .

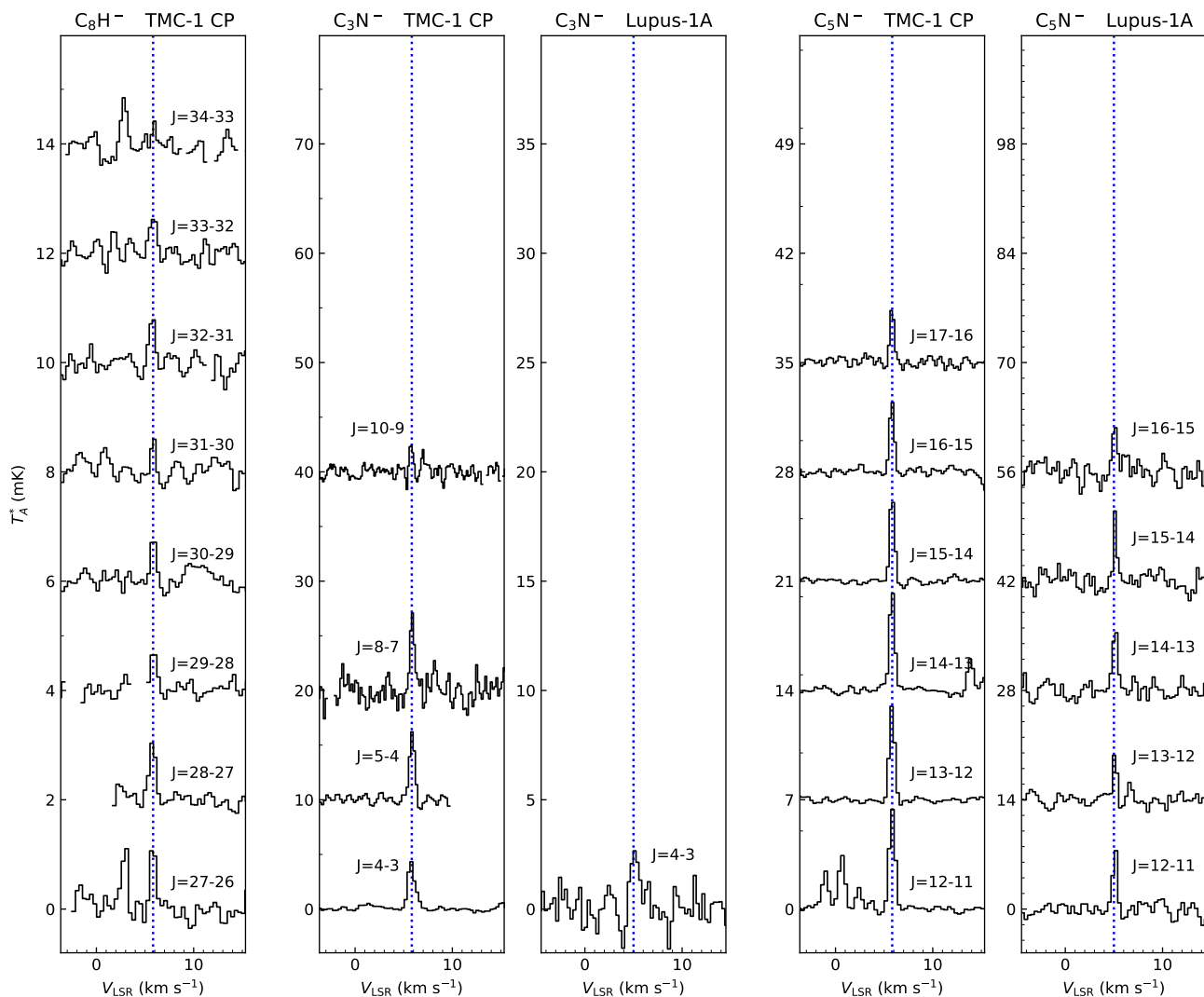


Fig. 3. Lines of C_8H^- observed toward TMC-1 CP and lines of the nitrile anions C_3N^- and C_5N^- observed toward TMC-1 CP and Lupus-1A using the Yebes 40m and IRAM 30m telescopes. See line parameters in Table A.1.

The velocity-integrated intensities of the lines of these species are given in Table A.2.

According to the literature, the most prevalent molecular anion, C_6H^- , has been detected in 11 cold dark clouds: TMC-1 CP (McCarthy et al. 2006), L1527 and Lupus-1A (Sakai et al. 2007, 2010), L1544 and L1521F (Gupta et al. 2009), and L1495B, L1251A, L1512, L1172, L1389, and TMC-1 C (Cordiner et al. 2011, 2013). All these detections were based on two individual or stacked lines lying in the frequency range 11–31 GHz (see Table A.1). Here we present additional lines of C_6H^- in the Q band for TMC-1 CP, Lupus-1A, L1527, L1495B, and L1544, together with the detection of C_6H^- in a new source, L483, through six lines lying in the Q band (see Fig. 1).

Molecular anions different to C_6H^- have turned out to be more difficult to detect as they have been only seen in a few sources. For example, C_4H^- has been only detected in three dark clouds, L1527 (Agúndez et al. 2008), Lupus-1A (Sakai et al. 2010), and TMC-1 CP (Cordiner et al. 2013). These detections rely on one or two lines (see Table A.1). Here we report the detection of two additional lines of C_4H^- in the Q band toward these three sources, together with the detection of C_4H^- in one new source, L483 (see Fig. 2).

The hydrocarbon anion C_8H^- has been observed in two interstellar sources. Brünken et al. (2007a) reported the detection of four lines in the 12–19 GHz frequency range toward TMC-1 CP, while Sakai et al. (2010) reported the detection of this anion in Lupus-1A through two stacked lines at 18.7 and 21.0 GHz (see Table A.1). Thanks to our Yebes 40m data, we present new lines of C_8H^- in the Q band toward TMC-1 CP (see Fig. 3).

Finally, the nitrile anions C_3N^- and C_5N^- have resulted to be quite elusive as they have been only seen in one cold dark cloud, TMC-1 CP (Cernicharo et al. 2020). Here we present the same lines of C_3N^- and C_5N^- reported in Cernicharo et al. (2020) in the Q band, but with improved signal-to-noise ratios, plus two additional lines of C_3N^- in the 3 mm band. We also present the detection of C_3N^- and C_5N^- in one additional source, Lupus-1A (see Fig. 3).

3. Physical parameters of the sources

The interstellar clouds where molecular anions have been detected are 12 in total and comprise cold dense cores in different evolutionary stages, such as starless, prestellar, and protostellar (see Table 1). The classification as protostellar cores is evident in the cases of L1527 and L483 as the targeted posi-

Table 1. Source parameters.

Source	Type		Δv (km s ⁻¹)	T _k (K)	Method	Ref	$n(\text{H}_2)$		
	Ref						(cm ⁻³)	Method	Ref
TMC-1 CP	starless	(1)	0.60	9	CH ₃ CCH, CH ₃ C ₄ H	(8)	1.0 × 10 ⁴	HC ₃ N with ¹³ C	(8)
Lupus-1A	starless	(2)	0.50	11	CH ₃ CCH	(8)	1.8 × 10 ⁴	HC ₃ N with ¹³ C	(8)
L1527	protostar	(3)	0.60	14	CH ₃ CCH	(3,8)	> 1 × 10 ⁵	HC ₃ N with ¹³ C	(8)
L483	protostar	(4)	0.52	12	CH ₃ CCH	(8)	5.6 × 10 ⁴	HC ₃ N with ¹³ C	(8)
L1495B	prestellar	(5)	0.50	9	CH ₃ CCH	(8)	1.6 × 10 ⁴	HCC ¹³ CN	(8)
L1544	prestellar	(5)	0.60	10	NH ₃ , C ¹⁷ O, SO ₂	(9,10,11)	2 × 10 ⁴	SO, SO ₂	(11,12)
L1521F	prestellar	(5)	0.45	9	CH ₃ CCH, NH ₃	(8,13)	1 × 10 ⁴	HCCNC	(8)
L1251A	protostar	(6)	0.40	10	HC ₃ N hfs	(6)	2.1 × 10 ⁴	HC ₃ N	(6)
L1512	starless	(5)	0.30	10	HC ₃ N hfs	(6)	2.6 × 10 ⁴	HC ₃ N	(6)
L1172	protostar	(7)	0.55	10	HC ₃ N hfs	(6)	7.5 × 10 ⁴	HC ₃ N	(6)
L1389	protostar	(6)	0.40	10	HC ₃ N hfs	(6)	5.2 × 10 ⁴	HC ₃ N	(6)
TMC-1 C	starless	(5)	0.18	10	HC ₃ N hfs	(6)	1.1 × 10 ⁴	HC ₃ N	(6)

References: (1) Suzuki et al. (1992). (2) Sakai et al. (2010). (3) Sakai et al. (2008). (4) Agúndez et al. (2019). (5) Crapsi et al. (2005). (6) Cordiner et al. (2013). (7) Visser et al. (2002). (8) This work (see text). (9) Tafalla et al. (2002). (10) Bacmann et al. (2002). (11) Vastel et al. (2018). (12) Punanova et al. (2018). (13) Codella et al. (1997).

tions are those of the infrared sources IRAS 04368+2557 and IRAS 18148–0440, respectively (Sakai et al. 2008; Agúndez et al. 2019). We also classified L1251A, L1172, and L1389 as protostellar sources based on the proximity of an infrared source (L1251A IRS3, CB17 MMS, and IRAS 21017+6742, respectively) to the positions targeted by Cordiner et al. (2013). The differentiation between starless and prestellar core is in some cases more ambiguous. In those cases we followed the criterion based on the N₂D⁺/N₂H⁺ column density ratio by Crapsi et al. (2005). In any case, for our purposes it is not very important whether a given core is starless or prestellar.

To study the abundance and excitation of molecular anions in these 12 interstellar sources through non-LTE calculations we need to know which are the physical parameters of the clouds, mainly the gas kinetic temperature and the H₂ volume density, but also the emission size of anions and the linewidth. The adopted parameters are summarized in Table 1.

Given that C₆H⁻ has not been mapped in any interstellar cloud to date, it is not known whether the emission of molecular anions in each of the 12 sources is extended compared to the telescope beam sizes, which are in the range 21–67'' for the Yebes 40m, IRAM 30m, and GBT telescopes at the frequencies targeted for the observations of anions. Therefore one has to rely on maps of related species. In the case of TMC-1 CP we assume that anions are distributed in the sky as a circle with a diameter of 80'' based on the emission distribution of C₆H mapped by Fossé et al. (2001). Recent maps carried out with the Yebes 40m telescope (Cernicharo et al. 2023b) support the previous results of Fossé et al. (2001). For the remaining 11 sources, the emission distribution of C₆H is not known and thus we assume that the emission of anions is extended with respect to the telescope beam. This assumption is supported by the extended nature of HC₃N emission in the cases of L1495B, L1251A, L1512, L1172, L1389, and TMC-1 C, according to the maps presented by Cordiner et al. (2013), and of multiple molecular species, including C₄H, in L1544, according to the maps reported by Spezzano et al. (2017).

The linewidth adopted for each source (see Table 1) was calculated as the arithmetic mean of the values derived for the lines of C₆H⁻ in the Q band for TMC-1 CP, Lupus-1A, L1527, L1495B, and L1544. In the case of L483 we adopted the value derived by Agúndez et al. (2019) from the analysis of all the lines in the 3 mm band. For L1521F, L1251A, L1512, L1172, and L1389 the adopted linewidths come from IRAM 30m obser-

vations of CH₃CCH in the 3 mm band (see Sect. 2.1). Finally, for TMC-1 C we adopted as linewidth that derived for HC₃N by Cordiner et al. (2013).

The gas kinetic temperature was determined for some of the sources from the $J=5-4$ and $J=6-5$ rotational transitions of CH₃CCH, which lie around 85.4 and 102.5 GHz, respectively. We have IRAM 30m data of these lines for TMC-1 CP, Lupus-1A, L483, L1495B, and L1521F, while for L1527 we used the data obtained with the Nobeyama 45m telescope by Yoshida et al. (2019). Typically, the $K=0$, 1, and 2 components are detected, which allow us to use the line intensity ratio between the $K=1$ and $K=2$ components, belonging to the E symmetry species, to derive the gas kinetic temperature. Since transitions with $\Delta K \neq 0$ are radiatively forbidden, the relative populations of the $K=1$ and $K=2$ levels are controlled by collisions with H₂ and thus are thermalized at the kinetic temperature of H₂. We do not use the $K=0$ component because it belongs to a different symmetry species, A , and interconversion between A and E species is expected to be slow in cold dense clouds and thus their relative populations may not necessarily reflect the gas kinetic temperature.

For TMC-1 CP we derive kinetic temperatures of 8.8 ± 0.6 K and 9.0 ± 0.6 K from the $J=5-4$ and $J=6-5$ lines of CH₃CCH, respectively. Similarly, using the $J=8-7$ through $J=12-11$ lines of CH₃C₄H, which lie in the Q band, we derive temperatures of 9.1 ± 0.7 K, 8.7 ± 0.6 K, 9.0 ± 0.6 K, 8.1 ± 0.7 K, and 9.1 ± 0.8 K, respectively. We thus adopt a gas kinetic temperature of 9 K, which is slightly lower than values derived in previous studies, 11.0 ± 1.0 K and 10.1 ± 0.9 K at two positions close to the cyanopolyne peak using NH₃ (Fehér et al. 2016) and 9.9 ± 1.5 K from CH₂CCH (Agúndez et al. 2022). In Lupus-1A we derive temperatures of 11.4 ± 1.7 K and 10.2 ± 1.1 K from the $J=5-4$ and $J=6-5$ lines of CH₃CCH, respectively. We thus adopt a gas kinetic temperature of 11 K, which is somewhat below the value of 14 ± 2 K derived in Agúndez et al. (2015) using the $K=0$, 1, and 2 components of the $J=5-4$ transition of CH₃CCH. In L1527 we derive 13.6 ± 2.5 K and 15.1 ± 2.4 K from the line parameters of CH₃CCH $J=5-4$ and $J=6-5$ reported by Yoshida et al. (2019). We thus adopt a kinetic temperature of 14 K, which agrees perfectly with the value of 13.9 K derived by Sakai et al. (2008) using CH₃CCH as well. The gas kinetic temperature in L483 has been estimated to be 10 K by Anglada et al. (1997) using NH₃, while Agúndez et al. (2019) derive values of 10 K and 15 ± 2 K using either ¹³CO or CH₃CCH. A new analysis of the

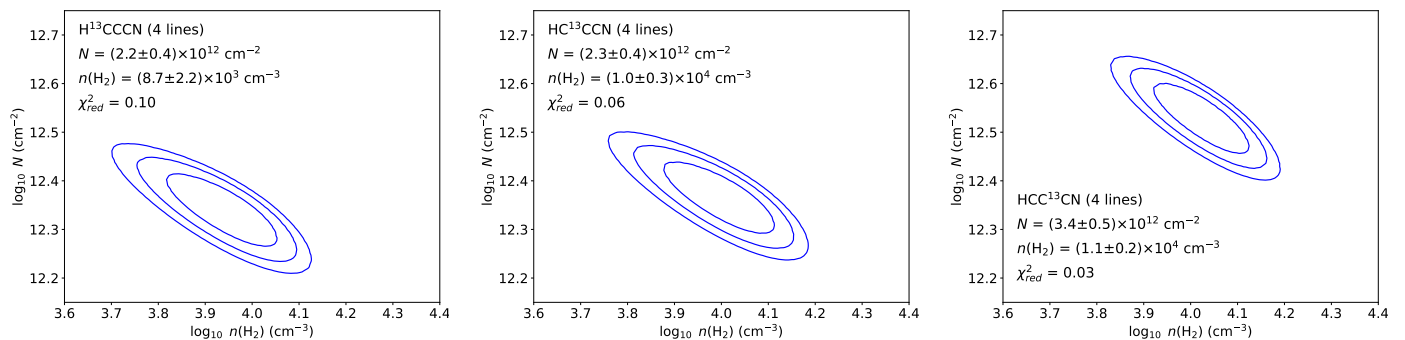


Fig. 4. χ^2 as a function of H_2 volume density and column density of each of the three ^{13}C isotopologues of HC_3N in TMC-1 CP. Contours correspond to 1, 2, and 3 σ levels. The three maps have the same scale in the x and y axes to facilitate the comparison. The column density of HCC^{13}CN is clearly higher than those of H^{13}CCCN and HC^{13}CCN . The volume density of H_2 is constrained to a very narrow range, $(0.9\text{--}1.1) \times 10^4 \text{ cm}^{-3}$, by the three ^{13}C isotopologues of HC_3N .

CH_3CCH data of Agúndez et al. (2019) in which the weak $K = 3$ components are neglected and only the $K = 1$ and $K = 2$ components are used results in kinetic temperatures of $11.5 \pm 1.1 \text{ K}$ and $12.6 \pm 1.5 \text{ K}$, depending on whether the $J = 5\text{--}4$ or $J = 6\text{--}5$ transition is used. We thus adopt a kinetic temperature of 12 K for L483. For L1495B we derive $9.1 \pm 0.9 \text{ K}$ and $9.2 \pm 0.7 \text{ K}$ from $\text{CH}_3\text{CCH } J = 5\text{--}4$ and $J = 6\text{--}5$, and we thus adopt a kinetic temperature of 9 K . In L1521F we also adopt a gas kinetic temperature of 9 K since the derived temperatures from $\text{CH}_3\text{CCH } J = 5\text{--}4$ and $J = 6\text{--}5$ are $9.0 \pm 0.7 \text{ K}$ and $8.9 \pm 0.9 \text{ K}$. The value agrees well with the temperature of $9.1 \pm 1.0 \text{ K}$ derived by Codella et al. (1997) using NH_3 . For the remaining cores, the gas kinetic temperatures were taken from the literature, as summarized in Table 1.

To estimate the volume density of H_2 we used the ^{13}C isotopologues of HC_3N when these data were available. We have Yebe 40m data of the $J = 4\text{--}3$ and $J = 5\text{--}4$ lines of H^{13}CCCN , HC^{13}CCN , and HCC^{13}CN for TMC-1 CP, Lupus-1A, L1527, and L483. Data for one or various lines of these three isotopologues in the 3 mm band are also available from the IRAM 30m telescope (see Sect. 2.1) or from the Nobeyama 45 telescope (for L1527; see Yoshida et al. 2019). Using the ^{13}C isotopologues of HC_3N turned out to constrain much better the H_2 density that using the main isotopologue because one gets rid of optical depth effects. We carried out non-LTE calculations under the Large Velocity Gradient (LVG) formalism adopting the gas kinetic temperature and linewidth given in Table 1 and varying the column density of the ^{13}C isotopologue of HC_3N and the H_2 volume density. As collision rate coefficients we used those calculated by Faure et al. (2016) for HC_3N with ortho and para H_2 , where we adopted a low ortho-to-para ratio of H_2 of 10^{-3} , which is theoretically expected for cold dark clouds (e.g., Flower et al. 2006). The exact value of the ortho-to-para ratio of H_2 is not very important as long as the para form is well in excess of the ortho form, so that collisions with para H_2 dominate. The best estimates for the column density of the ^{13}C isotopologue of HC_3N and the volume density of H_2 are found by minimizing χ^2 , which is defined as

$$\chi^2 = \sum_{i=1}^{N_l} \left[\frac{(I_{\text{calc}} - I_{\text{obs}})}{\sigma} \right]^2, \quad (1)$$

where the sum extends over the N_l lines available, I_{calc} and I_{obs} are the calculated and observed velocity-integrated brightness temperatures, and σ are the uncertainties in I_{obs} , which include the error given by the Gaussian fit and the calibration error of 10%. To evaluate the goodness of the fit, we use the reduced

χ^2 , which is defined as $\chi_{\text{red}}^2 = \chi_{\text{min}}^2 / (N_l - p)$, where χ_{min}^2 is the minimum value of χ^2 and p is the number of free parameters. Typically, a value of $\chi_{\text{red}}^2 \lesssim 1$ indicates a good quality of the fit. In this case we have $p = 2$ because there are two free parameters, the column density of the ^{13}C isotopologue of HC_3N and the H_2 volume density. Errors in these two parameters are given as 1σ , where for $p = 2$, the 1σ level (68% confidence) corresponds to $\chi^2 + 2.3$. The same statistical analysis is adopted in Sect. 5 when studying molecular anions and their neutral counterparts through the LVG method. In some cases in which the number of lines is small or the H_2 density is poorly constrained, the H_2 volume density is kept fixed. In those cases $p = 1$ and the 1σ error (68% confidence) in the column density is given by $\chi^2 + 1.0$.

In Fig. 4 we show the results for TMC-1 CP. In this starless core the H_2 volume density is well constrained by the four available lines of the three ^{13}C isotopologues of HC_3N to a narrow range of $(0.9\text{--}1.1) \times 10^4 \text{ cm}^{-3}$ with very low values of χ_{red}^2 . We adopt as H_2 density in TMC-1 CP the arithmetic mean of the values derived for the three isotopologues, i.e., $1.0 \times 10^4 \text{ cm}^{-3}$ (see Table 1). Similar calculations allow to derive H_2 volume densities of $1.8 \times 10^4 \text{ cm}^{-3}$ for Lupus-1A, $5.6 \times 10^4 \text{ cm}^{-3}$ for L483, and a lower limit of 10^5 cm^{-3} for L1527 (see Table 1). The value for L483 is of the same order than those derived in the literature, $3.4 \times 10^4 \text{ cm}^{-3}$ from the model of Jørgensen et al. (2002) and $3 \times 10^4 \text{ cm}^{-3}$, from either NH_3 (Anglada et al. 1997) or CH_3OH (Agúndez et al. 2019). For L1495B we could only retrieve data for one of the ^{13}C isotopologues of HC_3N , HCC^{13}CN , from which we derive a H_2 density of $1.6 \times 10^4 \text{ cm}^{-3}$ (see Table 1). In the case of L1521F, ^{13}C isotopologues of HC_3N were not available and thus we used lines of HCCNC , adopting the collision rate coefficients calculated by Bop et al. (2021), to derive a rough estimate of the H_2 volume density of $1 \times 10^4 \text{ cm}^{-3}$ (see Table 1). Higher H_2 densities, in the range $(1\text{--}5) \times 10^5 \text{ cm}^{-3}$, are derived for L1521F from N_2H^+ and N_2D^+ (Crapsi et al. 2005), probably because these molecules trace the innermost dense regions depleted in CO.

For the remaining sources we adopted H_2 volume densities from the literature (see Table 1). For L1544 we adopted a value of $2 \times 10^4 \text{ cm}^{-3}$ from the analysis of SO and SO_2 lines by Vastel et al. (2018). This H_2 density is in agreement with the range of values, $(1.5\text{--}4.0) \times 10^4 \text{ cm}^{-3}$, found by Bop et al. (2022) in their excitation analysis of HCCNC and HNC_3 . Note that H_2 volume densities toward the dust peak are larger than 10^6 cm^{-3} . However, as shown by Spezzano et al. (2017), the emission of C_4H probes the outer shells and thus a density of a few 10^4 cm^{-3} is appropriate for our calculations toward the CH_3OH peak. In

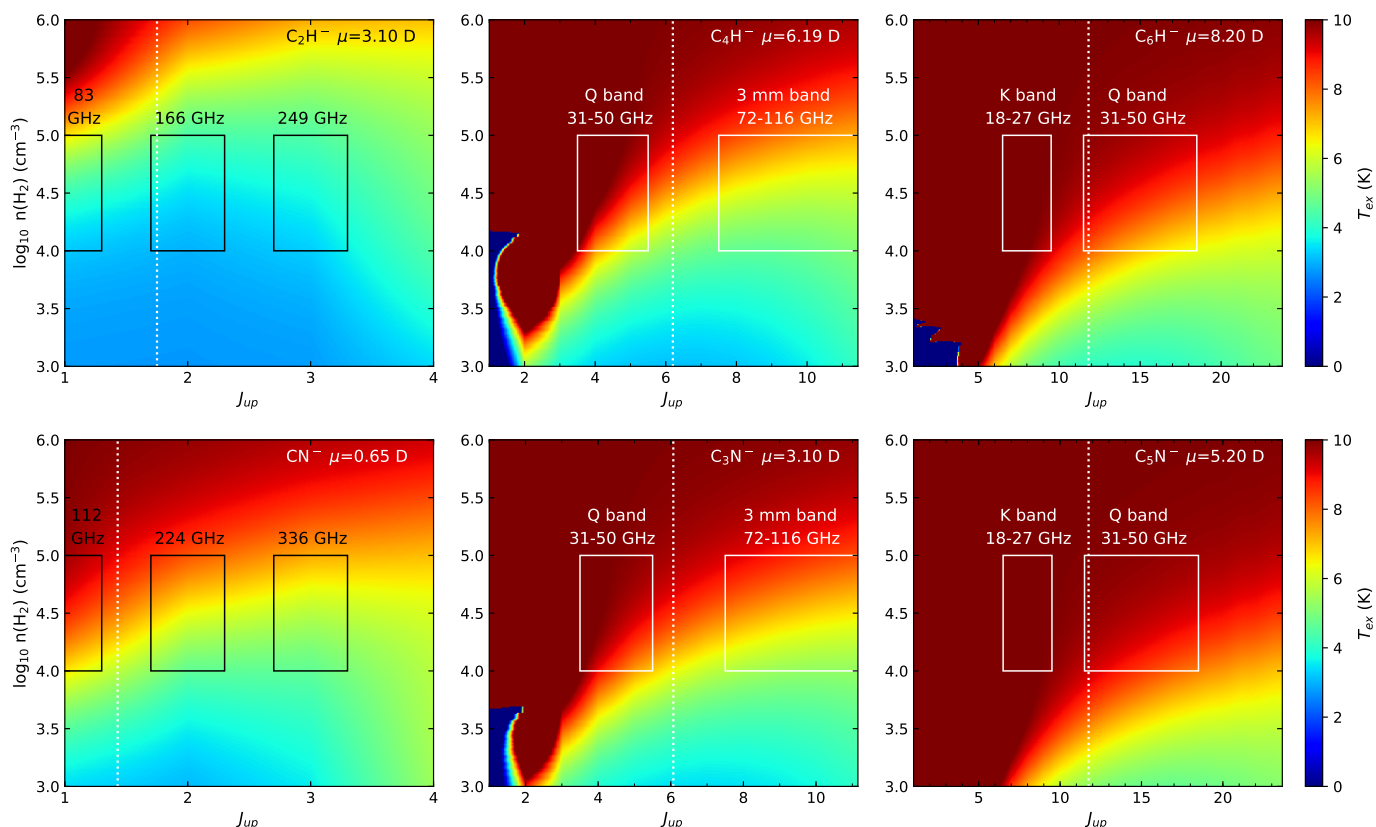


Fig. 5. Excitation temperature (color-coded map) as a function of quantum number of upper level (x-axis) and H_2 volume density (y-axis) for six negative molecular anions as obtained from LVG calculations adopting a gas kinetic temperature of 10 K, a column density of 10^{11} cm^{-2} , and a linewidth of 0.5 km s^{-1} . The references for the dipole moments are Brünken et al. (2007b) for C_2H^- , Botschwina (2000) for C_4H^- , Blanksby et al. (2001) for C_6H^- , Botschwina et al. (1995) for CN^- , Thaddeus et al. (2008) and Kotos et al. (2008) for C_3N^- , and Botschwina & Oswald (2008) for C_5N^- . For reference, the white dotted vertical line indicates the J level at which the energy is 10 K. The microwave and mm spectral regions observable with radiotelescopes are indicated. The small dark blue regions in the bottom-left corner of the C_4H^- , C_6H^- , and C_3N^- panels correspond to negative excitation temperatures.

the cases of L1251A, L1512, L1172, L1389, and TMC-1 C, we adopted the H_2 densities from the analysis of HC_3N lines by Cordiner et al. (2013). The reliability of the H_2 volume densities derived by these authors is supported by the fact that the densities they derive for TMC-1 CP and L1495B, $1.0 \times 10^4 \text{ cm}^{-3}$ and $1.1 \times 10^4 \text{ cm}^{-3}$, respectively, are close to the values determined in this study from ^{13}C isotopologues of HC_3N (see Table 1).

In spite of the different evolutionary status of the 12 anion-containing clouds, the gas kinetic temperatures and H_2 volume densities at the scales probed by the Yebes 40m, IRAM 30m, and GBT telescopes are not that different. Gas temperatures are restricted to the very narrow range 9–14 K, while H_2 densities are in the range $(1.0\text{--}7.5) \times 10^4 \text{ cm}^{-3}$, at the exception of L1527 which has an estimated density in excess of 10^5 cm^{-3} (see Table 1).

4. Excitation of anions: general considerations

One may expect that given the large dipole moments of molecular anions, as high as 10.4 D in the case of C_8H^- (Blanksby et al. 2001), the rotational levels should be populated out of thermodynamic equilibrium in cold dark clouds. This is not always the case as it will be shown here. To get insight into the excitation of negative molecular ions in interstellar clouds we run non-LTE calculations under the LVG formalism adopting typical parameters of cold dark clouds, i.e., a gas kinetic temperature of 10 K,

a column density of 10^{11} cm^{-2} (of the order of the values typically derived for anions in cold dark clouds; see references in Sect. 2.2), and a linewidth of 0.5 km s^{-1} (see Table 1), and we varied the volume density of H_2 between 10^3 and 10^6 cm^{-3} . The sets of rate coefficients for inelastic collisions with H_2 adopted are summarized in Table 2. In those cases in which only collisions with He are available we scaled the rate coefficients by multiplying them by the square root of the ratio of the reduced masses of the H_2 and He colliding systems. When inelastic collisions for ortho and para H_2 are available, we adopted a ortho-to-para ratio of H_2 of 10^{-3} .

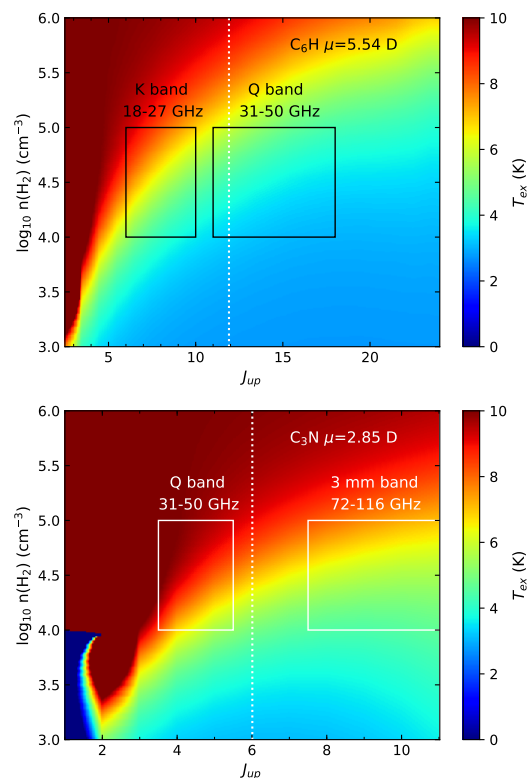
In Fig. 5 we show the calculated excitation temperatures (T_{ex}) of lines of molecular anions as a function of the quantum number J of the upper level and the H_2 volume density. The different panels correspond to different anions and show the regimes in which lines are either thermalized ($T_{\text{ex}} \sim 10 \text{ K}$) or subthermally excited ($T_{\text{ex}} < 10 \text{ K}$). To interpret these results it is useful to think in terms of the critical density, which for a given rotational level can be evaluated as the ratio of the de-excitation rates due to spontaneous emission and due to inelastic collisions (e.g., Lara-Moreno et al. 2019). Collision rate coefficients for transitions with $\Delta J = -1$ or -2 , which are usually the most efficient, are of the order of $10^{-10} \text{ cm}^3 \text{ s}^{-1}$ at a temperature of 10 K for the anions for which calculations have been carried out (see Table 2). The Einstein coefficient for spontaneous emission depends linearly on the square of the dipole moment and the cube of the

Table 2. Collision rate coefficients used in this study.

Species	Collision data available?	Adopted colliding system	Reference
Molecular anions			
C ₂ H ⁻	Yes	C ₂ H ⁻ – <i>p</i> -H ₂	Toumi et al. (2021)
C ₄ H ⁻	Yes	C ₄ H ⁻ – (<i>o/p</i>)-H ₂	Balança et al. (2021)
C ₆ H ⁻	Yes	C ₆ H ⁻ – (<i>o/p</i>)-H ₂	Walker et al. (2017)
C ₈ H ⁻	No	C ₆ H ⁻ – (<i>o/p</i>)-H ₂	Walker et al. (2017)
CN ⁻	Yes	CN ⁻ – (<i>o/p</i>)-H ₂	Kłos & Lique (2011)
C ₃ N ⁻	Yes	C ₃ N ⁻ – (<i>o/p</i>)-H ₂	Lara-Moreno et al. (2019)
C ₅ N ⁻	No	C ₆ H ⁻ – (<i>o/p</i>)-H ₂	Walker et al. (2017)
Radicals			
C ₄ H	No	HC ₃ N – (<i>o/p</i>)-H ₂	Faure et al. (2016)
C ₆ H	Yes	C ₆ H – He	Walker et al. (2018)
C ₈ H	No	HC ₅ N – <i>p</i> -H ₂ + IOS	Lique (priv. comm.) Alexander (1982)
C ₃ N	Yes	C ₃ N – He	Lara-Moreno et al. (2021)
C ₅ N	No	HC ₅ N – <i>p</i> -H ₂ + IOS	Lique (priv. comm.) Alexander et al. (1986)

frequency. Therefore, the critical density (and thus the degree of departure from LTE) is very different depending on the dipole moment of the anion and on the frequency of the transition. Regarding the dependence of the critical density on the dipole moment, C₂H⁻ and CN⁻ have a similar weight, and thus their low-*J* lines, which are the ones observable for cold clouds, have similar frequencies. However, these two anions have quite different dipole moments, 3.1 and 0.65 Debye, respectively (Brünken et al. 2007b; Botschwina et al. 1995), which make them to show a different excitation pattern. As seen in Fig. 5, the low-*J* lines of CN⁻ are in LTE at densities above 10⁵ cm⁻³ while those of C₂H⁻ require much higher H₂ densities to be in LTE. With respect to the dependence of the critical density with frequency, as one moves along the series of increasing weight C₂H⁻ → C₄H⁻ → C₆H⁻ or CN⁻ → C₃N⁻ → C₅N⁻ (see Fig. 5), the most favorable lines for detection in cold clouds (those with upper level energies around 10 K) shift to lower frequencies, which make the Einstein coefficients, and thus the critical densities, to decrease. That is, the lines of anions targeted by radiotelescopes are more likely to be thermalized for heavy anions than for light ones (see the higher degree of thermalization when moving from lighter to heavier anions in Fig. 5).

The volume densities of H₂ in cold dark clouds are typically in the range 10⁴-10⁵ cm⁻³ (see Table 1). Therefore, if C₂H⁻ is detected in a cold dark cloud at some point in the future, the most favorable line for detection, the *J* = 1-0, would be most likely subthermally excited, making necessary to use the collision rate coefficients to derive a precise abundance. In the case of a potential future detection of CN⁻ in a cold interstellar cloud, the *J* = 1-0 line would be in LTE only if the H₂ density of the cloud is ≥ 10⁵ cm⁻³ and out of LTE for lower densities (see Fig. 5). The medium-sized anions C₄H⁻ and C₃N⁻ are predicted to have their *Q* band lines more or less close to LTE depending on whether the H₂ density is closer to 10⁵ or to 10⁴ cm⁻³, while the lines in the 3 mm band are likely to be subthermally excited unless the H₂ density is above 10⁵ cm⁻³ (see Fig. 5). For the heavier anions C₆H⁻ and C₅N⁻, the lines in the *K* band are predicted to be thermalized at the gas kinetic temperature, while those in the *Q* band may or may not be thermalized depending on the H₂ density (see Fig. 5). Comparatively, the *Q* band lines of C₅N⁻ are more easily thermalized than those of C₆H⁻ because C₅N⁻ has a smaller dipole moment than C₆H⁻. We note that the results


Fig. 6. Same as Fig. 5 but for the radicals C₆H and C₃N adopting in this case a column density of 10¹² cm⁻². The references for the dipole moments are Woon (1995) for C₆H and McCarthy et al. (1995) for C₃N.

concerning C₅N⁻ have to be taken with caution because we used the collision rate coefficients calculated for C₆H⁻ in the absence of specific collision data for C₅N⁻ (see Table 2). We did similar calculations for C₈H⁻, C₁₀H⁻, and C₇N⁻ (not shown) using the collision rate coefficients of C₆H⁻. We find that the lines in a given spectral range deviate more from thermalization as the size of the anion increases. In the *K* band, the lines of C₆H⁻ and C₅N⁻ are thermalized, while those of C₁₀H⁻ become subthermally excited at low densities, around 10⁴ cm⁻³. In the *Q* band the deviation from thermalization is even more marked for these large anions.

In summary, non-LTE calculations are particularly important to derive accurate abundances for anions when just one or two lines are detected and these lie in a regime of subthermal excitation, as indicated in Fig. 5. This becomes critical, in order of decreasing importance, for C₂H⁻, CN⁻, C₄H⁻, C₃N⁻, C₆H⁻, C₈H⁻, and C₅N⁻ (for the three latter only if observed at frequencies above 30 GHz). The drawback is that the H₂ volume density must be known with a good precision if one aims at determining the anion column density accurately with only one or two lines.

In the case of the neutral counterparts of molecular anions, collision rate coefficients have been calculated for C₆H and C₃N with He as collider (Walker et al. 2018; Lara-Moreno et al. 2021). We thus carried out LVG calculations similar to those presented before for anions. In this case we adopt a higher column density of 10¹² cm⁻², in line with typical values in cold dark clouds (see references in Sect. 2.2). The results are shown in Fig. 6. It is seen that in the case of C₃N, the excitation pattern is similar to that of the corresponding anion, C₃N⁻, shown in Fig. 5. The thermalization of C₃N occurs at densities somewhat higher compared to C₃N⁻, mainly because the collision rate co-

Table 3. Results from LVG and rotation diagram analyses.

Source	Species	N_l^a	$n(\text{H}_2)$	N	χ_{red}^2	T_{rot} (K)	N	N	Ref
			(cm^{-3})	(cm^{-2})			(cm^{-2})	(cm^{-2})	
			LVG		Rotation diagram			Literature	
TMC-1 CP	C_6H^-	11	$(5.9 \pm 1.6) \times 10^3$	$(1.5 \pm 0.2) \times 10^{11}$	0.38	5.5 ± 0.3	$(2.3 \pm 0.4) \times 10^{11}$	1.0×10^{11}	(1)
TMC-1 CP	C_4H^-	2	5.9×10^3 ^b	$(2.1 \pm 0.2) \times 10^{10}$	–	5.5 ^b	2.4×10^{10}	8.0×10^9	(2)
TMC-1 CP	C_8H^-	12	$(1.8 \times 0.8) \times 10^4$	$(2.0 \pm 0.4) \times 10^{10}$	0.97	7.1 ± 0.5	$(2.7 \pm 0.7) \times 10^{10}$	2.1×10^{10}	(3)
TMC-1 CP	C_3N^-	4	$(1.5 \pm 0.6) \times 10^4$	$(6.4 \pm 0.8) \times 10^{10}$	0.04	6.0 ± 0.5	$(8.8 \pm 1.8) \times 10^{10}$	1.3×10^{11}	(4)
TMC-1 CP	C_5N^-	6	$(5.4 \times 2.3) \times 10^3$	$(8.8 \pm 1.4) \times 10^{10}$	0.44	6.6 ± 0.7	$(1.2 \pm 0.4) \times 10^{11}$	2.6×10^{11}	(4)
Lupus-1A	C_6H^-	8	$> 1.5 \times 10^4$	$(8.6 \pm 0.6) \times 10^{10}$	1.06	12.0 ± 1.5	$(8.8 \pm 1.5) \times 10^{10}$	6.5×10^{10}	(5)
Lupus-1A	C_4H^-	4	$(3.5 \pm 1.5) \times 10^4$	$(2.2 \pm 0.4) \times 10^{10}$	2.23	6.9 ± 0.9	$(3.2 \pm 0.9) \times 10^{10}$	4.4×10^{10}	(5)
Lupus-1A	C_8H^-	2	1.8×10^4 ^b	$(1.9 \pm 0.3) \times 10^{10}$	–	12.0 ^b	2.1×10^{10}		
Lupus-1A	C_3N^-	1	1.8×10^4 ^b	$(4.0 \pm 1.2) \times 10^{10}$	–	12.0 ^b	5.1×10^{10}		
Lupus-1A	C_5N^-	5	$> 3 \times 10^3$	$(5.5 \pm 0.8) \times 10^{10}$	1.52	12.0 ^b	5.8×10^{10}		
L1527	C_6H^-	8	$> 1 \times 10^4$	$(4.5 \pm 0.5) \times 10^{10}$	1.23	10.9 ± 1.7	$(5.4 \pm 1.4) \times 10^{10}$	5.8×10^{10}	(6)
L1527	C_4H^-	4	$> 7 \times 10^4$	$(1.5 \pm 0.2) \times 10^{10}$	0.18	16.1 ± 3.3	$(1.6 \pm 0.5) \times 10^{10}$	1.6×10^{10}	(7)
L483	C_6H^-	6	$> 1 \times 10^4$	$(2.0 \pm 0.3) \times 10^{10}$	1.03	12.0 ^b	2.1×10^{10}		
L483	C_4H^-	2	5.6×10^4 ^b	$(6.4 \pm 1.3) \times 10^9$	–	12.0 ^b	8.9×10^9		
L1495B	C_6H^-	7	$(2.3 \pm 1.0) \times 10^3$	$(4.5 \pm 1.7) \times 10^{10}$	1.62	5.0 ± 0.6	$(5.9 \pm 2.7) \times 10^{10}$	3.4×10^{10}	(2)
L1544	C_6H^-	5	$> 1 \times 10^3$	$(2.5 \pm 1.0) \times 10^{10}$	1.01	6.5 ± 1.6	$(3.2 \pm 1.8) \times 10^{10}$	3.1×10^{10}	(8)
L1521F	C_6H^-	1	1×10^4 ^b	$(3.4 \pm 0.8) \times 10^{10}$	–	9.0 ^b	4.2×10^{10}	3.4×10^{10}	(8)
L1251A	C_6H^-	2	2.1×10^4 ^b	$(2.2 \pm 0.4) \times 10^{10}$	–	10.0 ^b	2.5×10^{10}	2.3×10^{10}	(2)
L1512	C_6H^-	2	2.6×10^4 ^b	$(1.4 \pm 0.2) \times 10^{10}$	–	10.0 ^b	1.6×10^{10}	1.5×10^{10}	(2)
L1172	C_6H^-	2	7.5×10^4 ^b	$(2.4 \pm 0.3) \times 10^{10}$	–	10.0 ^b	2.5×10^{10}	2.4×10^{10}	(2)
L1389	C_6H^-	2	5.2×10^4 ^b	$(2.0 \pm 0.3) \times 10^{10}$	–	10.0 ^b	2.2×10^{10}	2.1×10^{10}	(2)
TMC-1 C	C_6H^-	2	1.1×10^4 ^b	$(4.5 \pm 0.5) \times 10^{10}$	–	10.0 ^b	5.2×10^{10}	4.8×10^{10}	(2)
TMC-1 CP	C_6H	17	$(7.5 \pm 2.8) \times 10^5$	$(4.8 \pm 0.2) \times 10^{12}$	3.60	7.0 ± 0.3	$(6.2 \pm 0.7) \times 10^{12}$	3.0×10^{12}	(6)
TMC-1 CP	C_4H	13	$(8.6 \pm 0.9) \times 10^3$	$(8.5 \pm 0.7) \times 10^{13}$	3.29	5.5 ± 0.1	$(1.05 \pm 0.07) \times 10^{14}$	7.1×10^{14}	(7)
TMC-1 CP	C_8H	21	1.0×10^4 ^b	$(3.0 \pm 0.1) \times 10^{11}$	2.86	6.8 ± 0.2	$(8.0 \pm 1.4) \times 10^{11}$	4.6×10^{11}	(3)
TMC-1 CP	C_3N	10	$(1.2 \pm 0.2) \times 10^4$	$(1.2 \pm 0.1) \times 10^{13}$	1.50	4.8 ± 0.1	$(1.7 \pm 0.2) \times 10^{13}$	1.8×10^{13}	(4)
TMC-1 CP	C_5N	12	$> 1 \times 10^3$	$(4.7 \pm 0.3) \times 10^{11}$	0.18	9.1 ± 0.9	$(4.8 \pm 1.0) \times 10^{11}$	6.0×10^{11}	(4)
Lupus-1A	C_6H	16	$> 7 \times 10^5$	$(3.7 \pm 0.2) \times 10^{12}$	1.11	10.7 ± 0.7	$(3.8 \pm 0.4) \times 10^{12}$	3.1×10^{12}	(5)
Lupus-1A	C_4H	10	$(1.2 \pm 0.2) \times 10^4$	$(8.4 \pm 0.9) \times 10^{13}$	1.56	7.3 ± 0.2	$(8.0 \pm 0.6) \times 10^{13}$	5.0×10^{14}	(5)
Lupus-1A	C_8H	2	1.8×10^4 ^b	$(2.7 \pm 0.4) \times 10^{11}$	–	10.7 ^b	2.8×10^{11}	3.5×10^{11}	(5)
Lupus-1A	C_3N	8	$(3.5 \pm 0.5) \times 10^4$	$(6.2 \pm 0.5) \times 10^{12}$	1.19	6.8 ± 0.2	$(8.1 \pm 0.8) \times 10^{12}$		
Lupus-1A	C_5N	10	1.8×10^4 ^b	$(3.1 \pm 0.2) \times 10^{11}$	1.38	7.6 ± 1.7	$(4.9 \pm 2.7) \times 10^{11}$		
L1527	C_6H	16	$> 1.5 \times 10^6$	$(8.8 \pm 0.4) \times 10^{11}$	0.66	19.6 ± 3.4	$(9.7 \pm 1.6) \times 10^{11}$	6.2×10^{11}	(6)
L1527	C_4H	10	$(1.4 \pm 0.6) \times 10^5$	$(2.9 \pm 0.1) \times 10^{13}$	0.29	13.4 ± 0.5	$(2.9 \pm 0.2) \times 10^{13}$	1.5×10^{14}	(7)
L483	C_6H	14	$(4.1 \pm 1.6) \times 10^5$	$(7.5 \pm 0.5) \times 10^{11}$	0.22	8.3 ± 0.6	$(8.7 \pm 1.5) \times 10^{11}$		
L483	C_4H	14	$(1.3 \pm 0.2) \times 10^4$	$(2.3 \pm 0.2) \times 10^{13}$	3.94	7.0 ± 0.1	$(3.0 \pm 0.2) \times 10^{13}$	1.2×10^{14}	(9)
L1495B	C_6H	16	$(7.0 \pm 2.8) \times 10^5$	$(1.5 \pm 0.1) \times 10^{12}$	1.04	7.0 ± 0.3	$(1.8 \pm 0.2) \times 10^{12}$	2.5×10^{12}	(2)
L1544	C_6H	11	$(1.6 \pm 0.7) \times 10^5$	$(8.7 \pm 1.5) \times 10^{11}$	1.19	5.4 ± 0.4	$(1.4 \pm 0.3) \times 10^{12}$	1.2×10^{12}	(8)
L1521F	C_6H	2	1×10^4 ^b	$(9.5 \pm 2.0) \times 10^{11}$	–	9.0 ^b	1.0×10^{12}	8×10^{11}	(8)
L1251A	C_6H	3	2.1×10^4 ^b	$(1.5 \pm 0.2) \times 10^{12}$	–	10.0 ^b	7.8×10^{11}	7.6×10^{11}	(2)
L1512	C_6H	5	2.6×10^4 ^b	$(7.6 \pm 0.6) \times 10^{11}$	–	10.0 ^b	5.5×10^{11}	4.6×10^{11}	(2)
L1172	C_6H	1	7.5×10^4 ^b	$(8.0 \pm 1.1) \times 10^{11}$	–	10.0 ^b	7.6×10^{11}	7.1×10^{11}	(2)
L1389	C_6H	3	5.2×10^4 ^b	$(4.4 \pm 0.6) \times 10^{11}$	–	10.0 ^b	5.0×10^{11}	4.7×10^{11}	(2)
TMC-1 C	C_6H	1	1.1×10^4 ^b	$(5.5 \pm 0.6) \times 10^{12}$	–	10.0 ^b	1.6×10^{12}	1.5×10^{12}	(2)

^a Number of lines included in the analysis.

^b Parameter was fixed to the value determined for a similar species, if possible, or to the value given in Table 1.

References: (1) McCarthy et al. (2006). (2) Cordiner et al. (2013). (3) Brünken et al. (2007a). (4) Cernicharo et al. (2020). (5) Sakai et al. (2010). (6) Sakai et al. (2007). (7) Agúndez et al. (2008). (8) Gupta et al. (2009). (9) Agúndez et al. (2019).

efficients calculated for C_3N with He (Lara-Moreno et al. 2021) are smaller than those computed for C_3N^- with para H_2 (Lara-Moreno et al. 2019). We note that this conclusion may change if the collision rate coefficients of C_3N with H_2 are significantly larger than the factor of 1.39 due to the change in the reduced mass when changing He by H_2 . In the case of C_6H however the excitation behavior is very different to that of C_6H^- (compare C_6H^- in Fig. 5 with C_6H in Fig. 6). The rotational levels of the radical are much more subthermally excited than those of the corresponding anion, with a difference in the critical density of about a factor of 30. This is a consequence of the much smaller

collision rate coefficients calculated for C_6H with He (Walker et al. 2018) compared to those calculated for C_6H^- with para H_2 (Walker et al. 2017), a difference that is well beyond the factor of 1.40 due to the change in the reduced mass when changing He by H_2 .

5. Anion abundances

We evaluated the column densities of molecular anions and their corresponding neutral counterparts in the 12 studied sources by carrying out LVG calculations similar to those described in

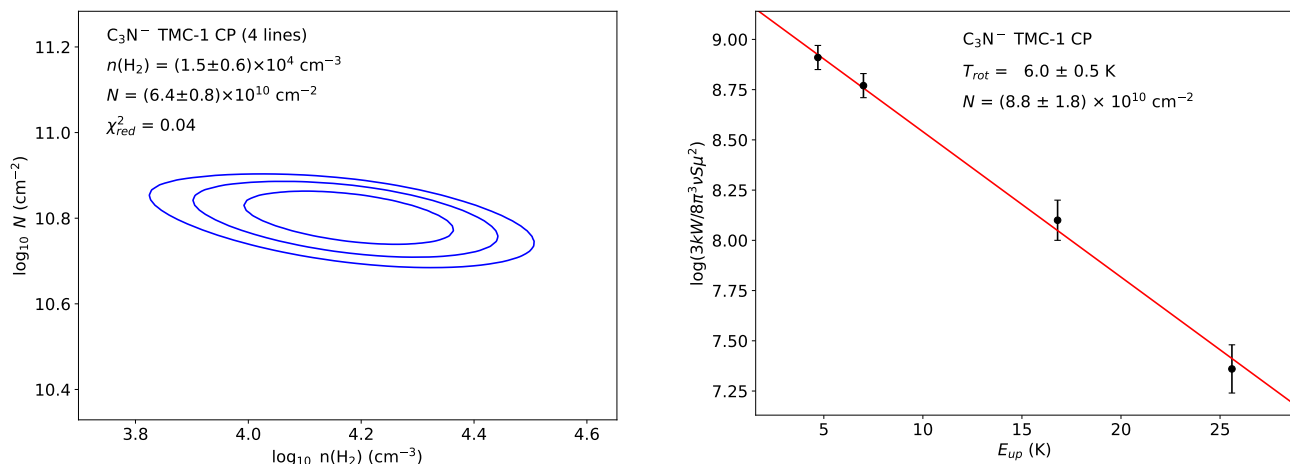


Fig. 7. Excitation and abundance analysis for C_3N^- in TMC-1 CP. The left panel shows χ^2 as a function of the H_2 volume density and the column density of C_3N^- , where contours correspond to 1, 2, and 3 σ levels. The right panel shows the rotation diagram.

Sect. 3 for the ^{13}C isotopologues of HC_3N . We used the collision rate coefficients given in Table 2. Gas kinetic temperatures and linewidths were fixed to the values given in Table 1, the ortho-para ratio of H_2 , when needed, was fixed to 10^{-3} , and both the column density of the species under study and the H_2 volume density were varied. The best estimates for these two parameters were found by minimization of χ^2 (see Sect. 3). In addition, to evaluate the rotational temperature, and thus the level of departure from LTE, and to have an independent estimate of the column density, we constructed rotation diagrams.

The LVG method should provide a more accurate determination of the column density than the rotation diagram, as long as the collision rate coefficients with para H_2 and the gas kinetic temperature are accurately known. If an independent determination of the H_2 volume density is available from some density tracer (in our case the ^{13}C isotopologues of HC_3N are used in several sources), a good agreement between the values of $n(H_2)$ obtained from the species under study and from the density tracer supports the reliability of the LVG analysis. We note that densities do not need to be similar if the species studied and the density tracer are distributed over different regions, although in our case we expect similar distributions for HC_3N , molecular anions, and their neutral counterparts, as long as all them are carbon chains. A low value of χ^2_{red} , typically $\lesssim 1$, is also indicative of the goodness of the LVG analysis. If the quality of the LVG analysis is not satisfactory or the collision rate coefficients are not accurate, a rotation diagram may still provide a good estimate of the column density if the number of detected lines is high enough and they span a wide range of upper level energies. Therefore, a high number of detected lines makes likely to end up with a correct determination of the column density. On the other hand, if only one or two lines are detected, the accuracy with which the column density can be determined relies heavily on whether the H_2 volume density, in the case of an LVG calculation, or the rotational temperature, in the case of the rotation diagram, are known with some confidence.

In Table 3 we present the results from the LVG analysis and the rotation diagram for all molecular anions detected in cold dark clouds and for the corresponding neutral counterparts, and compare the column densities derived with values from the literature, when available. In general, the column densities derived through the rotation diagram agree within 50%, with those derived by the LVG analysis. The sole exceptions are C_8H in TMC-1 CP and C_6H in TMC-1 C. In the former case, the lack of spe-

cific collision rate coefficients for C_8H probably introduces an uncertainty in the determination of the column density. In the case of C_6H in TMC-1 C, the suspected problem in the collision rate coefficients used for C_6H (see below) is probably behind the too large column density derived by the LVG method.

We first discuss the excitation and abundance analyses carried out for negative ions. For the anions detected in TMC-1 CP through more than two lines, i.e., C_6H^- , C_8H^- , C_3N^- , and C_5N^- , the quality of the LVG analysis is good (in Fig. 7 we show the case of C_3N^-). First, the number of lines available is sufficiently high and they cover a wide range of upper level energies. Second, the values of χ^2_{red} are $\lesssim 1$. And third, the H_2 densities derived are on the same order (within a factor of two) of that obtained through ^{13}C isotopologues of HC_3N . The rotational temperatures derived by the rotation diagram indicate subthermal excitation, which is consistent with the H_2 densities derived and the excitation analysis presented in Sect. 4. We note that the column densities derived by the rotation diagram are systematically higher,

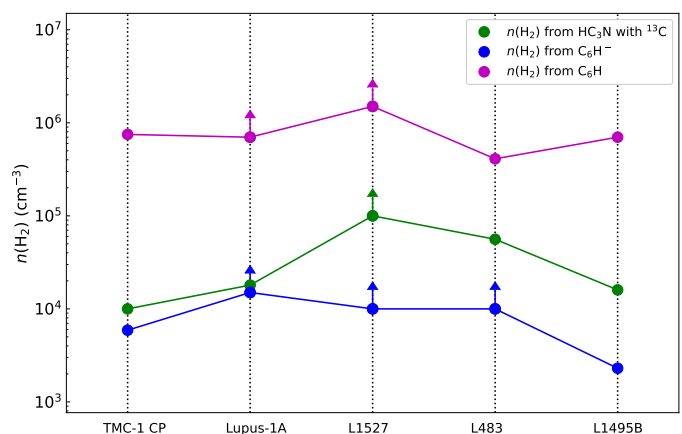


Fig. 8. Volume density of H_2 in various cold dark clouds determined through LVG calculations using different tracers. Green points correspond to densities derived from ^{13}C isotopologues of HC_3N (see values in Table 1), while blue and magenta points correspond to densities obtained from the anion C_6H^- and the radical C_6H , respectively (see values in Table 3). Note that H_2 densities derived through C_6H^- are close to those derived by ^{13}C isotopologues of HC_3N , while H_2 densities derived through C_6H are systematically higher by factors of 10-50.

Table 4. Recommended column densities and anion-to-neutral abundance ratios.

	N (cm ⁻²)	N (cm ⁻²)	Ratio (%)	Ratio (%)	Ref
		This work		Literature	
	C_4H^-	C_4H	C_4H^-/C_4H		
TMC-1 CP	$(2.1 \pm 0.6) \times 10^{10}$	$(8.5 \pm 2.6) \times 10^{13}$	0.025 ± 0.007	0.0012 ± 0.0004	(1)
Lupus-1A	$(2.2 \pm 0.7) \times 10^{10}$	$(8.4 \pm 1.3) \times 10^{13}$	0.026 ± 0.005	0.0088 ± 0.0053	(2)
L1527	$(1.5 \pm 0.2) \times 10^{10}$	$(2.9 \pm 0.4) \times 10^{13}$	0.052 ± 0.004	0.011	(3)
L483	$(6.4 \pm 1.9) \times 10^9$	$(2.3 \pm 0.3) \times 10^{13}$	0.028 ± 0.008		
	C_6H^-	C_6H	C_6H^-/C_6H		
TMC-1 CP	$(1.5 \pm 0.2) \times 10^{11}$	$(4.8 \pm 1.4) \times 10^{12}$	3.1 ± 0.6	2.5	(4)
Lupus-1A	$(8.6 \pm 1.3) \times 10^{10}$	$(3.7 \pm 1.1) \times 10^{12}$	2.3 ± 0.5	2.1 ± 0.6	(2)
L1527	$(4.5 \pm 0.7) \times 10^{10}$	$(8.8 \pm 2.6) \times 10^{11}$	5.1 ± 1.1	9.3 ± 2.9	(5)
L483	$(2.0 \pm 0.3) \times 10^{10}$	$(7.5 \pm 2.3) \times 10^{11}$	2.7 ± 0.6		
L1495B	$(4.5 \pm 1.4) \times 10^{10}$	$(1.5 \pm 0.5) \times 10^{12}$	3.0 ± 0.8	1.4 ± 0.2	(1)
L1544	$(2.5 \pm 0.8) \times 10^{10}$	$(8.7 \pm 2.6) \times 10^{11}$	2.9 ± 0.8	2.5 ± 0.8	(6)
L1521F	$(3.4 \pm 1.0) \times 10^{10}$	$(1.0 \pm 0.3) \times 10^{12}$	3.4 ± 1.0	4 ± 1	(6)
L1251A	$(2.2 \pm 0.7) \times 10^{10}$	$(7.8 \pm 2.3) \times 10^{11}$	2.8 ± 0.8	3.0 ± 0.6	(1)
L1512	$(1.4 \pm 0.4) \times 10^{10}$	$(5.5 \pm 1.7) \times 10^{11}$	2.5 ± 0.7	3.3 ± 0.4	(1)
L1172	$(2.4 \pm 0.7) \times 10^{10}$	$(7.6 \pm 2.3) \times 10^{11}$	3.2 ± 0.9	3.3 ± 0.5	(1)
L1389	$(2.0 \pm 0.6) \times 10^{10}$	$(5.0 \pm 1.5) \times 10^{11}$	4.0 ± 1.1	4.4 ± 0.8	(1)
TMC-1 C	$(4.5 \pm 1.4) \times 10^{10}$	$(1.6 \pm 0.5) \times 10^{12}$	2.8 ± 0.8	3.1 ± 0.3	(1)
	C_8H^-	C_8H	C_8H^-/C_8H		
TMC-1 CP	$(2.0 \pm 0.3) \times 10^{10}$	$(3.0 \pm 0.9) \times 10^{11}$	6.7 ± 1.4	5	(7)
Lupus-1A	$(1.9 \pm 0.6) \times 10^{10}$	$(2.7 \pm 0.8) \times 10^{11}$	7.0 ± 2.0	4.7 ± 1.7	(2)
	C_3N^-	C_3N	C_3N^-/C_3N		
TMC-1 CP	$(6.4 \pm 1.0) \times 10^{10}$	$(1.2 \pm 0.2) \times 10^{13}$	0.53 ± 0.04	0.71	(8)
Lupus-1A	$(4.0 \pm 1.2) \times 10^{10}$	$(6.2 \pm 0.9) \times 10^{12}$	0.65 ± 0.13		
	C_5N^-	C_5N	C_5N^-/C_5N		
TMC-1 CP	$(8.8 \pm 1.3) \times 10^{10}$	$(4.7 \pm 0.7) \times 10^{11}$	19 ± 1	43	(8)
Lupus-1A	$(5.5 \pm 0.8) \times 10^{10}$	$(3.1 \pm 0.5) \times 10^{11}$	18 ± 1		

References: (1) Cordiner et al. (2013). (2) Sakai et al. (2010). (3) Agúndez et al. (2008). (4) McCarthy et al. (2006). (5) Sakai et al. (2007). (6) Gupta et al. (2009). (7) Brünken et al. (2007a). (8) Cernicharo et al. (2020).

by $\sim 50\%$, compared to those derived through the LVG analysis. These differences are due to the breakdown of various assumptions made in the frame of the rotation diagram method, mainly the assumption of a uniform excitation temperature across all transitions and the validity of the Rayleigh-Jeans limit. Only the assumption that $\exp(h\nu/kT_{ex}) - 1 = h\nu/kT_{ex}$, implicitly made by the rotation diagram method in the Rayleigh-Jeans limit, already implies errors of 10-20% in the determination of the column density for these anions. We therefore adopt as preferred values for the column densities those derived through the LVG method and assign an uncertainty of 15%, which is the typical statistical error in the determination of the column density by the LVG analysis. The recommended values are given in Table 4. Based on the same arguments, we conclude that the LVG analysis is satisfactory for C_6H^- and C_5N^- in Lupus-1A, C_6H^- and C_4H^- in L1527, and C_6H^- in L483, and thus adopt the column densities derived by the LVG method with the same estimated uncertainty of 15% (see Table 4). In other cases the LVG analysis is less reliable due to a variety of reasons: only one or two lines are available (C_4H^- in TMC-1 CP, C_8H^- and C_3N^- in Lupus-1A, C_4H^- in L483, and C_6H^- in the clouds L1521F, L1251A, L1512, L1172, L1389, and TMC-1 C), the parameter χ_{red}^2 is well above unity (C_4H^- in Lupus-1A), or the column density has a sizable error (C_6H^- in L1495B and L1544). In those cases we adopt the

column densities derived by the LVG method but assign a higher uncertainty of 30% (values are given in Table 4).

In order to derive anion-to-neutral abundance ratios, we applied the same analysis carried out for the anions to the corresponding neutral counterparts. We first focus on the radical C_6H . There is one striking issue in the LVG analysis carried out for this species: the H_2 volume densities derived through C_6H are systematically higher, by 1-2 orders of magnitude, than those derived through the ^{13}C isotopologues of HC_3N (see Fig. 8). This fact, together with the previous marked difference in the excitation pattern compared to that of C_6H^- discussed in Sect. 4, suggests that the collision coefficients adopted for C_6H , which are based on the $C_6H - He$ system studied by Walker et al. (2018), are too small. A further problem when using the collision coefficients of Walker et al. (2018) is that the line intensities from the $^2\Pi_{1/2}$ state, which in TMC-1 CP are around 100 times smaller than those of the $^2\Pi_{3/2}$ state, are overestimated by a factor of ~ 10 . All these issues indicate that it is worth to undertake calculations of the collision rate coefficients of C_6H with H_2 . The suspected problem in the collision rate coefficients of C_6H make us to adopt a conservative uncertainty of 30% in the column densities derived. Moreover, in those sources in which C_6H is observed through just a few lines (L1521F, L1251A, L1512, L1172, L1389, and TMC-1 C) we need to fix the H_2 density to the values derived through other density tracer (see Table 1), and

given the marked difference between the H_2 densities derived through C_6H and other density tracers, it is likely that the C_6H column densities derived by the LVG method are unreliable. In these cases we therefore adopted as preferred C_6H column densities those obtained from the rotation diagram (see Table 4). For the other neutral radicals, we adopted the column densities derived by the LVG method with an estimated uncertainty of 15 % when the LVG analysis was satisfactory (C_3N and C_5N in TMC-1 CP, C_4H , C_3N , and C_5N in Lupus-1A, and C_4H in L1527) and a higher uncertainty of 30 % otherwise (C_4H and C_8H in TMC-1 CP, C_8H in Lupus-1A, and C_4H in L483).

The recommended column densities for molecular anions and their neutral counterparts, and the corresponding anion-to-neutral ratios, are given in Table 4. Since the lines of a given anion and its corresponding neutral counterpart where in most cases observed simultaneously, we expect the error due to calibration to cancel when computing anion-to-neutral ratios. We therefore subtracted the 10 % error due to calibration in the column densities when computing errors in the anion-to-neutral ratios. In general, the recommended anion-to-neutral abundance ratios agree within 50 % with the values reported in the literature, when available. Higher differences, of up to a factor of two, are found for C_6H^- in L1527 and L1495B and for C_5N^- in TMC-1 CP. The most drastic differences are found for the C_4H^-/C_4H abundance ratio, for which we derive values much higher than those reported in the literature. The differences are largely due to the fact that here we adopt a revised value of the dipole moment of C_4H (2.10 D; Oyama et al. 2020), which is significantly higher than the value of 0.87 D calculated by Woon (1995) and adopted in previous studies. This fact makes the column densities of C_4H to be revised downward by a factor of ~ 6 , and consequently the C_4H^-/C_4H ratios are also revised upward by the same factor.

6. Discussion

Having at hand a quite complete observational picture of negative ions in the interstellar medium, as summarized in Table 4, it is interesting to examine which lessons can be learnt from this. There are at least two interesting aspects to discuss. First, how do the anion-to-neutral abundance ratio behave from one source to another, and whether the observed variations can be related to some property of the cloud. And second, within a given source, how do the anion-to-neutral abundance ratio vary for the different anions, and whether this can be related to the formation mechanism of anions.

Regarding the first point, since C_6H^- is the most widely observed anion, it is very convenient to focus on it to investigate the source-to-source behavior of negative ions. The detection of C_6H^- in L1527 and the higher C_6H^-/C_6H ratio derived in that source compared to that in TMC-1 CP led Sakai et al. (2007) to suggest that this was a consequence of the higher H_2 density in L1527 compared to TMC-1 CP. This point was later on revisited by Cordiner et al. (2013) with a larger number of sources detected in C_6H^- . These authors found a trend in which the C_6H^-/C_6H ratio increases with increasing H_2 density and further argued that this ratio increases as the cloud evolves from quiescent to star-forming, with ratios below 3 % in quiescent sources and above that value in star-forming ones.

There are theoretical grounds that support a relationship between the C_6H^-/C_6H ratio and the H_2 density. Assuming that the formation of anions is dominated by radiative electron attachment to the neutral counterpart and that they are mostly destroyed through reaction with H atoms, as expected for the con-

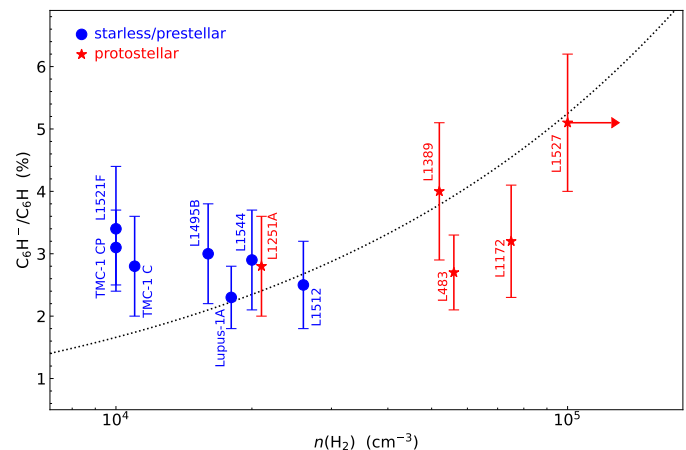


Fig. 9. Anion-to-neutral ratio C_6H^-/C_6H (see values in Table 4) as a function of H_2 volume density. We do not give errors in the H_2 densities because this parameter is not derived in a coherent way for all sources (see Table 1). The dotted line represents the trend expected according to theory (see text).

ditions of cold dense clouds (Flower et al. 2007), it can be easily shown that at steady state the anion-to-neutral abundance ratio is proportional to the abundance ratio between electrons and H atoms, which in turn is proportional to the square root of the H_2 volume density (e.g., Flower et al. 2007). That is,

$$\frac{C_6H^-}{C_6H} \propto \frac{e^-}{H} \propto n(H_2)^{1/2}. \quad (2)$$

In Fig. 9 we plot the observed C_6H^-/C_6H ratio as a function of the H_2 density for the 12 clouds where this anion has been detected. This is an extended and updated version of Figure 5 of Cordiner et al. (2013), where we superimpose the theoretical trend expected according to Eq. (2). In general terms, the situation depicted by Fig. 9 is not that different from that found by Cordiner et al. (2013). The main difference concerns L1495B, for which we derive a higher C_6H^-/C_6H ratio, 3.0 % instead of 1.4 %. Our value should be more accurate, given the larger number of lines used here. Apart from that, the C_6H^-/C_6H ratio tends to be higher in those sources with higher H_2 densities, which tend to be more evolved. This behavior is similar to that found by Cordiner et al. (2013). The data points in Fig. 9 seem to be consistent with the theoretical expectation. We however caution that there is substantial dispersion in the data points. Moreover, the uncertainties in the anion-to-neutral ratios, together with those affecting the H_2 densities (not shown), make it difficult to end up with a solid conclusion on whether or not observations follow the theoretical expectations. If we restrict to the five best characterized sources (TMC-1 CP, Lupus-1A, L1527, L483, and L1495B), all them observed in C_6H^- through four or more lines and studied in the H_2 density in a coherent way, then the picture is such that all sources, regardless of its H_2 density, have similar C_6H^-/C_6H ratios, at the exception of L1527, which remains the only data point supporting the theoretical relation between anion-to-neutral ratio and H_2 density. It is also worth noting that when looking at C_4H^- , L1527 shows also an enhanced anion-to-neutral ratio compared to TMC-1 CP, Lupus-1A, and L483. Further detections of C_6H^- in sources with high H_2 densities, preferably above 10^5 cm^{-3} , should help to shed light on the suspected relation between anion-to-neutral ratio and H_2 density. This however may not be easy because chemical models predict that, although the C_6H^-/C_6H ratio increases with increasing H_2

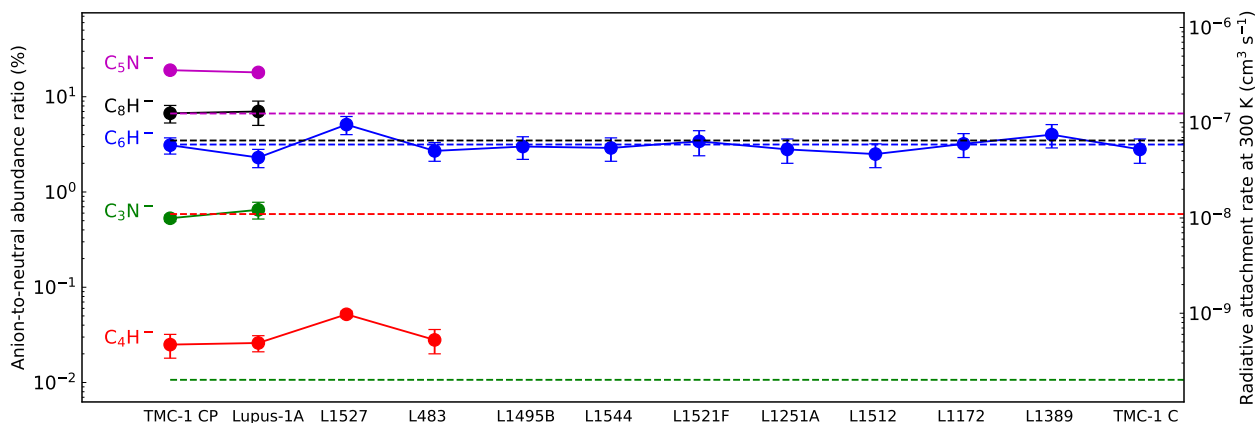


Fig. 10. Observed anion-to-neutral abundance ratios (referred to the left y axis) in cold interstellar clouds where molecular anions have been detected to date. Values are given in Table 4. Referred to the right y axis and following the same color code we also plot as dotted horizontal lines the calculated rate coefficients at 300 K for the reaction of radiative electron attachment to the neutral counterpart. Adopted values are $1.1 \times 10^{-8} \text{ cm}^3 \text{ s}^{-1}$ for C_4H , $6.2 \times 10^{-8} \text{ cm}^3 \text{ s}^{-1}$ for C_6H and C_8H (Herbst & Osamura 2008; they are shown slightly displaced for visualization purposes), $2.0 \times 10^{-10} \text{ cm}^3 \text{ s}^{-1}$ for C_3N (Petrie & Herbst 1997; Harada & Herbst 2008), and $1.25 \times 10^{-7} \text{ cm}^3 \text{ s}^{-1}$ for C_5N (Walsh et al. 2009). The scale of the right y axis is chosen to make the rate coefficient of electron attachment to C_6H to coincide with the mean of $\text{C}_6\text{H}^-/\text{C}_6\text{H}$ ratios and to cover the same range in logarithmic scale than the left y axis, which allows to visualize any potential proportionality between anion-to-neutral ratio and radiative electron attachment rate.

density, an increase in the density also brings a decrease in the column density of both C_6H and C_6H^- (Cordiner & Charnley 2012).

The second aspect that is worth to discuss is the variation of the anion-to-neutral ratio for different anions within a given source. Unlike the former source-to-source case, where variations were small (a factor of two at most), here anion-to-neutral ratios vary by orders of magnitude, i.e., well above uncertainties. Figure 10 summarizes the observational situation of interstellar anions in terms of abundances relative to their neutral counterpart. The variation of the anion-to-neutral ratios across different anions is best appreciated in TMC-1 CP and Lupus-1A, which stand out as the two most prolific sources of interstellar anions. The lowest anion-to-neutral ratio is reached by far for C_4H^- , while the highest values are found for C_5N^- and C_8H^- . We caution that the $\text{C}_5\text{N}^-/\text{C}_5\text{N}$ ratio could have been overestimated if the true dipole moment of C_5N is a mixture between those of the $^2\Sigma$ and $^2\Pi$ states, as discussed by Cernicharo et al. (2008), in a case similar to that studied for C_4H by Oyama et al. (2020). For the large anion C_7N^- , the anion-to-neutral ratio is not known in TMC-1 CP but it is probably large, as suggested by the detection of the lines of the anion and the non detection of the lines of the neutral (Cernicharo et al. 2023a). In the case of the even larger anion C_{10}H^- , the anion is found to be even more abundant than the neutral in TMC-1 CP by a factor of two, although this result has probably an important uncertainty since the detection is done by line stack (Remijan et al. 2023). Moreover, it is yet to be confirmed that the species identified is C_{10}H^- and not C_9N^- (Pardo et al. 2023). In any case, a solid conclusion from the TMC-1 CP and Lupus-1A data shown in Fig. 10 is that when looking at either the hydrocarbon series of anions or at the nitrile series, the anion-to-neutral ratio clearly increases with increasing size. The most straightforward interpretation of this behavior is related to the formation mechanism originally proposed by Herbst (1981), which relies on the radiative electron attachment (REA) to the neutral counterpart and for which the rate coefficient is predicted to increase markedly with increasing molecular size.

If electron attachment is the dominant formation mechanism of anions and destruction rates are similar for all anions, we ex-

pect the anion-to-neutral abundance ratio to be proportional to the rate coefficient of radiative electron attachment. That is,

$$\frac{A^-}{A} \propto k_{\text{REA}}, \quad (3)$$

where A^- and A are the anion and its corresponding neutral counterpart, respectively, and k_{REA} is the rate coefficient for radiative electron attachment to A .

To get insight into this relation we plot in Fig. 10 the rate coefficients calculated for the reactions of electron attachment forming the different anions on a scale designed on purpose to visualize if observed anion-to-neutral ratios scale with calculated electron attachment rates. We arbitrarily choose C_6H^- as the reference for the discussion. If we first focus on the largest anion C_8H^- , we see that the $\text{C}_8\text{H}^-/\text{C}_8\text{H}$ ratios are systematically higher, by a factor of 2-3, than the $\text{C}_6\text{H}^-/\text{C}_6\text{H}$ ones, while Herbst & Osamura (2008) calculate identical electron attachment rates for C_6H and C_8H . Similarly, the $\text{C}_5\text{N}^-/\text{C}_5\text{N}$ ratios are higher, by a factor of 6-8 than the $\text{C}_6\text{H}^-/\text{C}_6\text{H}$ ratios, while the electron attachment rate calculated for C_5N is twice of that computed for C_6H in the theoretical scenario of Herbst & Osamura (2008). That is, for the large anions C_8H^- and C_5N^- there is a deviation of a factor of 2-4 from the theoretical expectation given by Eq. (3). This deviation is small given the various sources of uncertainties in both the observed anion-to-neutral ratio (mainly due to uncertainties in the dipole moments) and the calculated electron attachment rate coefficient. The situation is different for the medium size anions C_4H^- and C_3N^- . In the case of C_4H^- , anion-to-neutral ratios are ~ 100 times lower than for C_6H^- , while the electron attachment rate calculated for C_4H is just ~ 6 times lower than that computed for C_6H . The deviation from Eq. (3) of a factor ~ 20 , which is significant, is most likely due to the electron attachment rate calculated for C_4H by Herbst & Osamura (2008) being too large. In the case of C_3N^- , the observed anion-to-neutral ratios are 4-6 times lower than those derived for C_6H^- , while the electron attachment rate calculated by Petrie & Herbst (1997) for C_3N is 300 times lower than that computed for C_6H by Herbst & Osamura (2008). Here the deviation is as large as two orders of magnitude and it is probably caused by

the too low electron attachment rate calculated for C_3N . In summary, calculated electron attachment rates are consistent with observed anion-to-neutral ratios for the large species but not for the medium-sized species C_4H and C_3N , in which cases calculated rates are too large by a factor of ~ 20 and too small by a factor of ~ 100 , respectively.

Of course, the above conclusion holds in the scenario of anion formation dominated by electron attachment and similar destruction rates for all anions, which may not be strictly valid. For example, it has been argued (Douguet et al. 2015; Khamesian et al. 2016; Forer et al. 2023) that the process of radiative electron attachment is much less efficient than calculated by Herbst & Osamura (2008), with rate coefficients that are too small to sustain the formation of anions in interstellar space. Millar et al. (2017) discuss this point making the difference between direct and indirect radiative electron attachment, where for long carbon chains the direct process would be slow, corresponding to the rates calculated by Khamesian et al. (2016), while the indirect process could be fast if a long-lived superexcited anion is formed, something that has some experimental support. Millar et al. (2017) conclude that there are enough grounds to support rapid electron attachment to large carbon chains, as calculated by Herbst & Osamura (2008). The formation mechanism of anions through electron attachment is very selective for large species and thus has the advantage of naturally explaining the marked dependence of anion-to-neutral ratios with molecular size illustrated in Fig. 10, something that would be difficult to explain through other formation mechanism. Indeed, mechanisms such as dissociative electron attachment to metastable isomers such as HNC_3 and H_2C_6 (Petrie & Herbst 1997; Sakai et al. 2007) or reactions of H^- with polyynes and cyanopolyynes (Vuitton et al. 2009; Martínez et al. 2010; Khamesian et al. 2016; Gianturco et al. 2016; Murakami et al. 2022) could contribute to some extent but are unlikely to control the formation of anions since they can hardly explain why large anions are far more abundant than small ones.

7. Conclusions

We reported new detections of molecular anions in cold dense clouds and considerably expanded the number of lines through which negative ions are detected in interstellar clouds. The most prevalent anion remains to be C_6H^- , which to date has been seen in 12 interstellar clouds, while the rest of interstellar anions are observed in just 1-4 sources.

We carried out excitation calculations, which indicate that subthermal excitation is common for the lines of interstellar anions observed with radiotelescopes, with the low frequency lines of heavy anions being the easiest to thermalize. Important discrepancies between calculations and observations are found for the radical C_6H , which suggest that the collision rate coefficients currently available for this species need to be revisited.

We analyzed all the observational data acquired here and in previous studies through non-LTE LVG calculations and rotation diagrams to constrain the column density of each anion in each source. Differences in the anion-to-neutral abundance ratios with respect to literature values are small, less than 50% in general and up to a factor of two in a few cases. The highest difference is found for the C_4H^-/C_4H ratio, which is shifted upward with respect to previous values due to the adoption of a higher dipole moment for the radical C_4H .

The observational picture of interstellar anions brought by this study shows two interesting results. On the one side, the C_6H^-/C_6H ratio seems to be higher in clouds with a higher H_2

density, which is usually associated to a later evolutionary status of the cloud, although error bars make it difficult to clearly distinguish this trend. On the other hand, there is a very marked dependence of the anion-to-neutral ratio with the size of the anion, which is in line with the formation scenario involving radiative electron attachment, the theory of which must still be revised for medium size species such as C_4H and C_3N .

Acknowledgements. We acknowledge funding support from Spanish Ministerio de Ciencia e Innovación through grants PID2019-106110GB-I00, PID2019-107115GB-C21, and PID2019-106235GB-I00.

References

- Agúndez, M., Cernicharo, J., Guélin, M., et al. 2008, *A&A*, 478, L19
 Agúndez, M., Cernicharo, J., Guélin, M., et al. 2010, *A&A*, 517, L2
 Agúndez, M., Cernicharo, J., & Guélin, M. 2015, *A&A*, 577, L5
 Agúndez, M., Marcelino, N., Cernicharo, J., et al. 2019, *A&A*, 625, A147
 Agúndez, M., Marcelino, N., Cabezas, C., et al. 2022, *A&A*, 657, A96
 Agúndez, M., Roncero, O., Marcelino, N., et al. 2023, *A&A*, in press
 Alexander, M. H. 1982, *J. Chem. Phys.*, 76, 5974
 Alexander, M. H., Smedley, J. E., & Corey, G. C. 1986, *J. Chem. Phys.*, 84, 3049
 Anglada, G., Sepúlveda, I., & Gómez, J. F. 1997, *A&AS*, 121, 255
 Bacmann, A., Lefloch, B., Ceccarelli, C., et al. 2002, *A&A*, 389, L6
 Balança, C., Quintas-Sánchez, E., Dawes, R., et al. 2021, *MNRAS*, 508, 1148
 Biswas, R., Giri, K., González-Sánchez, L. et al. 2023, *MNRAS*, 522, 5775
 Blanksby, S. J., McAnoy, A. M., Dua, S., & Bowie, J. H. 2001, *MNRAS*, 328, 89
 Bop, C. T., Lique, F., Faure, A., et al. 2021, *MNRAS*, 501, 1911
 Bop, C. T., Desrousseaux, B., & Lique, F. 2022, *A&A*, 662, A102
 Botschwina, P., Seeger, S., Mladenovic, M., et al. 1995, *Int. Rev. Phys. Chem.*, 14, 169
 Botschwina, P. 2000, 55th Ohio Symposium on Molecular Spectroscopy, TC06
 Botschwina, P. & Oswald, R. 2008, *J. Chem. Phys.*, 129, 044305
 Brünken, S., Gupta, H., Gottlieb, C. A., et al. 2007a, *ApJ*, 664, L43
 Brünken, S., Gottlieb, C. A., Gupta, H., et al. 2007b, *A&A*, 464, L33
 Cabezas, C., Agúndez, M., Marcelino, N., et al. 2021, *A&A*, 654, A45
 Cabezas, C., Agúndez, M., Marcelino, N., et al. 2022, *A&A*, 657, L4
 Carelli, F., Satta, M., Grassi, T., & Gianturco, F. A. 2013, *ApJ*, 774, 97
 Cernicharo, J., Guélin, M., Agúndez, M., et al. 2007, *A&A*, 467, L37
 Cernicharo, J., Guélin, M., Agúndez, M., et al. 2008, *ApJ*, 688, L83
 Cernicharo, J., Marcelino, N., Roueff, E., et al. 2012, *ApJ*, 759, L43
 Cernicharo, J., Marcelino, N., Pardo, J. R., et al. 2020, *A&A*, 641, L9
 Cernicharo, J., Agúndez, M., Kaiser, R. L., et al. 2021, *A&A*, 652, L9
 Cernicharo, J., Pardo, J. R., Cabezas, C., et al. 2023a, *A&A*, 670, L19
 Cernicharo, J., Tercero, B., Marcelino, N., et al. 2023b, *A&A*, submitted
 Codella, C., Welsch, R., Henkel, C., et al. 1997, *A&A*, 324, 203
 Cordiner, M. A., Charnley, S. B., Buckle, J. V., et al. 2011, *ApJ*, 730, L18
 Cordiner, M. A. & Charnley, S. B. 2012, *ApJ*, 749, 120
 Cordiner, M. A., Buckle, J. V., Wirstrom, E. S., et al. 2013, *ApJ*, 770, 48
 Crapsi, A., Caselli, P., Walmsley, C. M., et al. 2005, *ApJ*, 619, 379
 Douguet, N., Fonseca dos Santos, S., Raoult, M., et al. 2015, *J. Chem. Phys.*, 142, 234309
 Dumouchel, F., Spielfiedel, A., Senent, M. L., & Feautrier, N. 2012, *Chem. Phys. Lett.*, 533, 6
 Dumouchel, F., Quintas-Sánchez, E., Balança, C., et al. 2023, *J. Chem. Phys.*, 158, 164307
 Faure, A., Lique, A., & Wiesenfeld, L. 2016, *MNRAS*, 460, 2103
 Fehér, O., Tóth, L. V., Ward-Thompson, D., et al. 2016, *A&A*, 590, A75
 Flower, D. R., Pineau des Forêts, G., & Walmsley, C. M. 2006, *A&A*, 449, 621
 Flower, D. R., Pineau des Forêts, G., & Walmsley, C. M. 2007, *A&A*, 474, 923
 Forer, J., Kokouline, V., & Stoecklin, T. 2023, *Phys. Rev. A*, 107, 043117
 Fossé, D., Cernicharo, J., Gerin, M., & Cox, P. 2001, *ApJ*, 552, 168
 Franz, J., Mant, B. P., González-Sánchez, L., et al. 2020, *J. Chem. Phys.*, 152, 234303
 Frayer, D. T., Ghigo, F., & Maddalena, R. J. 2018, GBT Memo #301
 Gianturco, F. A., Satta, M., Mendolicchio, M., et al. 2016, *ApJ*, 830, 2
 Gianturco, F. A., González-Sánchez, L., Mant, B. P., & Wester, R. 2019, *J. Chem. Phys.*, 151, 144304
 González-Sánchez, L., Mant, B. P., Wester, R., & Gianturco, F. A. 2020, *ApJ*, 897, 75
 Gottlieb, C. A., Brünken, S., McCarthy, M. C., & Thaddeus, P. 2007, *J. Chem. Phys.*, 126, 191101
 Gupta, H., Brünken, S., Tamassia, F., et al. 2007, *ApJ*, 655, L57
 Gupta, H., Gottlieb, C. A., McCarthy, M. C., & Thaddeus, P. 2009, *ApJ*, 691, 1494
 Harada, N. & Herbst, E. 2008, *ApJ*, 685, 272

- Herbst, E. 1981, *Nature*, 289, 656
- Herbst, E. & Osamura, Y. 2008, *ApJ*, 679, 1670
- Jiménez-Serra, I., Vasyunin, A. I., Caselli, P., et al. 2016, *ApJ*, 830, L6
- Jørgensen, J. K., Schöier, F. L., & van Dishoeck, E. F. 2002, *A&A*, 389, 908
- Khamesian, M., Douguet, N., Fonseca dos Santos, S., et al. 2016, *Phys. Rev. Lett.*, 117, 123001
- Klos, J. & Lique, F. 2011, *MNRAS*, 418, 271
- Kolos, R., Gronowski, M., & Botschwina, P. 2008, *J. Chem. Phys.*, 128, 154305
- Lara-Moreno, M., Stoecklin, T., & Halvick, P. 2017, *MNRAS*, 467, 4174
- Lara-Moreno, M., Stoecklin, T., & Halvick, P. 2019, *MNRAS*, 486, 414
- Lara-Moreno, M., Stoecklin, T., & Halvick, P. 2021, *MNRAS*, 507, 4086
- McCarthy, M. C., Gottlieb, C. A., Thaddeus, P., et al. 1995, *J. Chem. Phys.*, 103, 7820
- McCarthy, M. C., Gottlieb, C. A., Gupta, H., & Thaddeus, P. 2006, *ApJ*, 652, L141
- Marcelino, N., Cernicharo, J., Agúndez, M., et al. 2007, *ApJ*, 665, L127
- Martínez Jr., O., Yang, Z., Demarais, N. J., et al. 2010, *ApJ*, 720, 173
- Millar, T. J., Walsh, C., & Field, T. A. 2017, *Chem. Rev.*, 117, 1765
- Murakami, T., Iida, R., Hashimoto, Y., et al. 2022, *J. Phys. Chem. A*, 126, 9244
- Oyama, T., Ozaki, H., Sumiyoshi, Y., et al. 2020, *ApJ*, 890, 39
- Pardo, J. R., Cabezas, C., Agúndez, M., et al. 2023, *A&A*, submitted
- Petrie, S. & Herbst, E. 1997, *ApJ*, 491, 210
- Punanova, A., Caselli, P., Feng, S., et al. 2018, *ApJ*, 855, 112
- Remijan, A. J., Hollis, J. M., Lovas, F. J., et al. 2007, *ApJ*, 664, L47
- Remijan, A., Scolati, H. N., Burkhardt, A. M., et al. 2023, *ApJ*, 944, L45
- Sakai, N., Sakai, T., Osamura, Y., & Yamamoto, S. 2007, *ApJ*, 667, L65
- Sakai, N., Sakai, T., Hirota, T., & Yamamoto, S. 2008, *ApJ*, 672, 371
- Sakai, N., Shiino, T., Hirota, T., et al. 2010, *ApJ*, 718, L49
- Senent, M. L., Dayou, F., Dumouchel, F., et al. 2019, *MNRAS*, 486, 422
- Spezzano, S., Caselli, P., Bizzocchi, L., et al. 2017, *A&A*, 606, A82
- Suzuki, H., Yamamoto, S., Ohishi, M., et al. 1992, *ApJ*, 392, 551
- Tafalla, M., Myers, P. C., Caselli, P., et al. 2002, *ApJ*, 569, 815
- Tchakoua, T., Motapon, O., & Nsangou, M. 2018, *J. Phys. B: At. Mol. Opt. Phys.*, 51, 045202
- Tercero, F., López-Pérez, J. A., Gallego, J. D., et al. 2021, *A&A*, 645, A37
- Thaddeus, P., Gottlieb, C. A., Gupta, H., et al. 2008, *ApJ*, 677, 1132
- Toumi, I., Yazidi, O., & Najjar, F. 2021, *RSC Adv.*, 11, 13579
- Vastel, C., Quénard, D., Le Gal, R., et al. 2018, *MNRAS*, 478, 5514
- Visser, A. E., Richer, J. S., & Chandler, C. J. 2002, *ApJ*, 124, 2756
- Vuitton, V., Lavvas, P., Yelle, R. V., et al. 2009, *Planet. Space Sci.*, 57, 1558
- Walker, K. M., Dumouchel, F., Lique, F., & Dawes, R. 2016, *J. Chem. Phys.*, 145, 024314
- Walker, K. M., Lique, F., Dumouchel, F., & Dawes, R. 2017, *MNRAS*, 466, 831
- Walker, K. M., Lique, F., & Dawes, R. 2018, *MNRAS*, 473, 1407
- Walsh, C., Harada, N., Herbst, E., Millar, T. J. 2009, *ApJ*, 700, 752
- Woon, D. E. 1995, *Chem. Phys. Lett.*, 244, 45
- Yoshida, K., Sakai, N., Nishimura, Y., et al. 2019, *PASJ*, 71, S18

Appendix A: Supplementary table

Table A.1. Observed line parameters of molecular anions in interstellar clouds.

Species	Transition	Frequency (MHz)	V_{LSR} (km s ⁻¹)	Δv (km s ⁻¹)	T_A^* peak ^a (mK)	$\int T_A^* dv^a$ (mK km s ⁻¹)	Telescope	Reference	
TMC-1 CP									
C ₆ H ⁻	4-3	11014.896	+5.80(2)	0.38(4)	25(3)	10.1(33)	GBT	McCarthy et al. (2006)	
	5-4	13768.614	+5.80(11)	0.44(7)	24(3)	11.2(43)	GBT	McCarthy et al. (2006)	
	10-9	27537.130	{				41.6(90) ^{b,c}	GBT	Cordiner et al. (2013)
	11-10	30290.813							
	12-11	33044.488							
	13-12	35798.153	+5.78(1)	0.73(1)	22.3(23)	17.4(18)	Yebes 40m	This work	
	14-13	38551.808	+5.78(1)	0.70(1)	20.9(22)	15.5(17)	Yebes 40m	This work	
	15-14	41305.453	+5.79(2)	0.64(2)	18.9(20)	12.8(14)	Yebes 40m	This work	
	16-15	44059.085	+5.79(2)	0.56(3)	17.2(19)	10.3(12)	Yebes 40m	This work	
17-16	46812.706	+5.79(2)	0.57(3)	12.8(15)	7.7(10)	Yebes 40m	This work		
18-17	49566.313	+5.81(2)	0.59(4)	9.6(13)	6.0(8)	Yebes 40m	This work		
		49566.313	+5.84(3)	0.56(5)	5.4(10)	3.2(5)	Yebes 40m	This work	
C ₄ H ⁻	2-1	18619.761	+5.70(5)	0.43(13)		1.0(3) ^{b,d}	GBT	Cordiner et al. (2013)	
	4-3	37239.410	+5.81(2)	0.71(2)	6.0(7)	4.5(6)	Yebes 40m	This work	
	5-4	46549.156	+5.81(2)	0.55(3)	5.8(8)	3.4(4)	Yebes 40m	This work	
C ₈ H ⁻	11-10	12833.460	+5.71(5)	0.36(4)	8(1)	3.1(10)	GBT	Brünken et al. (2007a)	
	12-11	14000.134	+5.86(5)	0.37(4)	7(1)	2.8(10)	GBT	Brünken et al. (2007a)	
	13-12	15166.806	+5.84(6)	0.45(4)	6(1)	2.9(10)	GBT	Brünken et al. (2007a)	
	16-15	18666.814	+5.80(7)	0.34(5)	10(2)	3.6(16)	GBT	Brünken et al. (2007a)	
	27-26	31500.029	+5.82(4)	0.63(10)	1.28(28)	0.86(20)	Yebes 40m	This work	
	28-27	32666.670	+5.76(3)	0.76(6)	1.08(26)	0.87(15)	Yebes 40m	This work	
	29-28	33833.309	+5.90(12)	0.68(17)	0.78(19)	0.56(18)	Yebes 40m	This work	
	30-29	34999.944	+5.86(6)	0.60(10)	0.87(20)	0.56(14)	Yebes 40m	This work	
	31-30	36166.576	+5.83(8)	0.32(20)	1.01(24)	0.34(10)	Yebes 40m	This work	
	32-31	37333.205	+5.73(5)	0.66(11)	0.87(23)	0.61(16)	Yebes 40m	This work	
	33-32	38499.831	+5.81(9)	0.82(17)	0.68(20)	0.60(18)	Yebes 40m	This work	
	34-33	39666.453	+5.93(10)	0.40(12)	0.44(21)	0.19(7) ^e	Yebes 40m	This work	
	C ₃ N ⁻	4-3	38812.797	+5.78(1)	0.88(2)	4.2(2)	3.9(5)	Yebes 40m	This work
5-4		48515.872	+5.86(2)	0.61(4)	6.3(9)	4.1(6)	Yebes 40m	This work	
8-7		77624.540	+5.88(3)	0.52(8)	7.1(17)	3.9(9)	IRAM 30m	This work	
10-9		97029.687	+5.77(4)	0.38(6)	2.7(8)	1.1(3)	IRAM 30m	This work	
C ₅ N ⁻	12-11	33332.570	+5.83(1)	0.71(3)	6.5(7)	4.9(6)	Yebes 40m	This work	
	13-12	36110.238	+5.80(1)	0.64(2)	6.1(7)	4.1(5)	Yebes 40m	This work	
	14-13	38887.896	+5.81(1)	0.63(2)	6.5(8)	4.4(5)	Yebes 40m	This work	
	15-14	41665.541	+5.82(2)	0.58(2)	5.7(7)	3.5(5)	Yebes 40m	This work	
	16-15	44443.173	+5.79(2)	0.56(2)	4.7(6)	2.8(4)	Yebes 40m	This work	
	17-16	47220.793	+5.81(2)	0.50(4)	3.6(6)	1.9(3)	Yebes 40m	This work	
Lupus-1A									
C ₆ H ⁻	7-6	19276.037	+5.046(8)	0.16(2)	85(8) ^b	14(2) ^b	GBT	Sakai et al. (2010)	
	8-7	22029.741	+5.034(10)	0.17(2)	94(11) ^b	15(3) ^b	GBT	Sakai et al. (2010)	
	12-11	33044.488	+5.06(2)	0.59(3)	30.1(37)	18.9(24)	Yebes 40m	This work	
	13-12	35798.153	+5.08(2)	0.51(3)	32.9(40)	17.8(25)	Yebes 40m	This work	
	14-13	38551.808	+5.05(2)	0.48(4)	30.4(38)	15.7(20)	Yebes 40m	This work	
	15-14	41305.453	+5.09(3)	0.40(7)	32.7(42)	13.8(19)	Yebes 40m	This work	
	16-15	44059.085	+5.07(3)	0.55(6)	24.2(35)	14.2(22)	Yebes 40m	This work	
17-16	46812.706	+5.10(6)	0.51(8)	17.1(33)	9.3(18)	Yebes 40m	This work		
C ₄ H ⁻	4-3	37239.410	+5.078(13)	0.34(3)	59(5) ^b	19(5) ^b	GBT	Sakai et al. (2010)	
	4-3	37239.410	+5.04(4)	0.78(7)	7.4(14)	6.1(11)	Yebes 40m	This work	
	5-4	46549.156	+5.05(9)	0.45(12)	9.8(27)	4.7(13)	Yebes 40m	This work	
	9-8	83787.297	+5.23(6)	0.47(12)	10.4(31)	5.3(13)	IRAM 30m	This work	
C ₈ H ⁻	16-15	18666.814	{	+5.014(11)	0.09(3)	35(9)	4(1) ^{b,c}	GBT	Sakai et al. (2010)
	18-17	21000.145							
C ₃ N ⁻	4-3	38812.797	+5.16(15)	0.96(15)	2.8(10)	2.8(9)	Yebes 40m	This work	
C ₅ N ⁻	12-11	33332.570	+5.11(7)	0.50(9)	8.4(16)	4.4(10)	Yebes 40m	This work	
	13-12	36110.238	+5.11(7)	0.44(9)	6.5(13)	3.1(7)	Yebes 40m	This work	
	14-13	38887.896	+5.13(7)	0.64(8)	8.0(17)	5.4(11)	Yebes 40m	This work	
	15-14	41665.541	+5.14(9)	0.37(10)	9.2(19)	3.7(9)	Yebes 40m	This work	
	16-15	44443.173	+5.09(10)	0.58(15)	6.1(18)	3.8(11)	Yebes 40m	This work	
L1527									
C ₆ H ⁻	7-6	19276.037	+5.93(9)	0.45(11)	14(3) ^b	7(2) ^b	GBT	Sakai et al. (2007)	
	8-7	22029.741	+5.89(3)	0.49(10)	26(4) ^b	18(4) ^b	GBT	Sakai et al. (2007)	

Table A.1. continued.

Species	Transition	Frequency (MHz)	V_{LSR} (km s ⁻¹)	$\Delta\nu$ (km s ⁻¹)	T_A^* peak ^a (mK)	$\int T_A^* dv^a$ (mK km s ⁻¹)	Telescope	Reference
	12-11	33044.488	+5.90(5)	0.85(10)	9.6(14)	8.6(16)	Yebes 40m	This work
	13-12	35798.153	+5.85(4)	0.60(4)	11.4(20)	7.3(18)	Yebes 40m	This work
	14-13	38551.808	+5.84(3)	0.61(5)	12.0(18)	7.8(12)	Yebes 40m	This work
	15-14	41305.453	+5.90(3)	0.60(4)	16.4(25)	10.4(19)	Yebes 40m	This work
	16-15	44059.085	+5.90(3)	0.52(4)	14.5(23)	8.0(16)	Yebes 40m	This work
	17-16	46812.706	+5.83(5)	0.58(8)	11.1(23)	6.8(14)	Yebes 40m	This work
C ₄ H ⁻	4-3	37239.410	+5.92(12)	0.80(20)	3.2(10)	2.7(7)	Yebes 40m	This work
	5-4	46549.156	+6.05(15)	0.73(15)	4.9(19)	3.8(13)	Yebes 40m	This work
	9-8	83787.297	+5.80(3)	0.62(9)	13(2)	8(1)	IRAM 30m	Agúndez et al. (2008)
	10-9	93096.550	+5.90(4)	0.59(9)	11(2)	7(1)	IRAM 30m	Agúndez et al. (2008)
L483								
C ₆ H ⁻	12-11	33044.488	+5.38(6)	0.66(8)	4.9(11)	3.4(8)	Yebes 40m	This work
	13-12	35798.153	+5.33(5)	0.70(7)	5.8(10)	4.3(8)	Yebes 40m	This work
	14-13	38551.808	+5.33(5)	0.78(7)	5.2(9)	4.3(9)	Yebes 40m	This work
	15-14	41305.453	+5.29(6)	0.46(9)	5.3(12)	2.6(6)	Yebes 40m	This work
	16-15	44059.085	+5.24(10)	0.75(12)	4.8(12)	3.8(10)	Yebes 40m	This work
	17-16	46812.706	+5.34(7)	0.63(9)	5.0(14)	3.4(9)	Yebes 40m	This work
C ₄ H ⁻	4-3	37239.410	+5.39(8)	0.73(12)	2.8(7)	2.2(5)	Yebes 40m	This work
	5-4	46549.156	+5.37(10)	0.44(15)	2.7(12)	1.3(5) ^e	Yebes 40m	This work
L1495B								
C ₆ H ⁻	10-9	27537.130				9.6(20) ^{b,c}	GBT	Cordiner et al. (2013)
	11-10	30290.813						
	12-11	33044.488	+7.66(5)	0.80(7)	5.9(12)	5.0(9)	Yebes 40m	This work
	13-12	35798.153	+7.65(5)	0.50(8)	5.8(12)	3.1(6)	Yebes 40m	This work
	14-13	38551.808	+7.58(7)	0.39(10)	4.3(11)	1.8(4)	Yebes 40m	This work
	15-14	41305.453	+7.66(10)	0.36(14)	6.6(16)	2.6(6)	Yebes 40m	This work
	16-15	44059.085	+7.61(8)	0.49(12)	4.1(11)	2.1(6)	Yebes 40m	This work
L1544								
C ₆ H ⁻	7-6	19276.037 ^e	+7.08(3)	0.16(3)	16(2)	6.0(18)	GBT	Gupta et al. (2009)
			+7.30(3)	0.13(3)	26(2)			
	12-11	33044.488	+7.11(13)	0.67(28)	4.5(16)	3.2(14)	Yebes 40m	This work
	13-12	35798.153	+7.04(10)	0.48(16)	4.1(12)	2.1(9)	Yebes 40m	This work
	14-13	38551.808	+6.98(8)	0.50(13)	6.0(16)	3.2(12)	Yebes 40m	This work
	15-14	41305.453	+7.34(18)	0.76(36)	4.6(15)	3.7(16)	Yebes 40m	This work
L1521F								
C ₆ H ⁻	7-6	19276.037 ^e	+6.33(5)	0.18(3)	17(2)	7.0(17)	GBT	Gupta et al. (2009)
			+6.64(5)	0.35(9)	9(2)			
L1251A								
C ₆ H ⁻	10-9	27537.130				6.5(17) ^{b,c}	GBT	Cordiner et al. (2013)
	11-10	30290.813						
L1512								
C ₆ H ⁻	10-9	27537.130				4.3(8) ^{b,c}	GBT	Cordiner et al. (2013)
	11-10	30290.813						
L1172								
C ₆ H ⁻	10-9	27537.130				6.7(15) ^{b,c}	GBT	Cordiner et al. (2013)
	11-10	30290.813						
L1389								
C ₆ H ⁻	10-9	27537.130				5.9(14) ^{b,c}	GBT	Cordiner et al. (2013)
	11-10	30290.813						
TMC-1 C								
C ₆ H ⁻	10-9	27537.130				13.6(25) ^{b,c}	GBT	Cordiner et al. (2013)
	11-10	30290.813						

^a Unless otherwise stated, the intensity scale is antenna temperature (T_A^*). It can be converted to main beam brightness temperature (T_{mb}) by dividing by $B_{\text{eff}}/F_{\text{eff}}$, where B_{eff} is the main beam efficiency and F_{eff} is the telescope forward efficiency. For the Yebes 40m telescope in the Q band $B_{\text{eff}} = 0.797 \exp[-(\nu(\text{GHz})/71.1)^2]$ and $F_{\text{eff}} = 0.97$ (https://rt40m.oan.es/rt40m_en.php), for the IRAM 30m telescope $B_{\text{eff}} = 0.871 \exp[-(\nu(\text{GHz})/359)^2]$ and $F_{\text{eff}} = 0.95$ (<https://publicwiki.iram.es/Iram30mEficiencias>), and for the GBT telescope we adopt $F_{\text{eff}} = 1.0$ and $B_{\text{eff}} = 1.32 \times 0.71 \exp[-(\nu(\text{GHz})/103.7)^2]$ (Frayer et al. 2018). The error in $\int T_A^* dv$ includes the contributions from the Gaussian fit and from calibration (assumed to be 10%). ^b Intensity scale is T_{mb} . ^c Average of two lines. ^d Line neglected in the analysis. Intensity should be ~ 3 times larger to be consistent with the other lines. ^e Line detected marginally.

Table A.2. Observed velocity-integrated line intensities of neutral counterparts of molecular anions in interstellar clouds.

Species	Transition	Frequency (MHz)	$\int T_A^* dv$ (mK km s ⁻¹) ^a	Telescope	Reference
TMC-1 CP					
C ₆ H	² Π _{3/2} J = 15/2 – 13/2 a	20792.907	133(24) ^b	GBT	Sakai et al. (2007)
	² Π _{3/2} J = 15/2 – 13/2 b	20794.475	112(22) ^b	GBT	Sakai et al. (2007)
	² Π _{3/2} J = 21/2 – 19/2 a	29109.658	332.4(420) ^b	GBT	Cordiner et al. (2013)
	² Π _{3/2} J = 23/2 – 21/2 a	31881.860	175.6(176)	Yebes 40m	This work
	² Π _{3/2} J = 23/2 – 21/2 b	31885.541	173.5(175)	Yebes 40m	This work
	² Π _{3/2} J = 25/2 – 23/2 a	34654.037	158.9(160)	Yebes 40m	This work
	² Π _{3/2} J = 25/2 – 23/2 b	34658.383	158.5(160)	Yebes 40m	This work
	² Π _{3/2} J = 27/2 – 25/2 a	37426.192	141.5(180)	Yebes 40m	This work
	² Π _{3/2} J = 27/2 – 25/2 b	37431.255	141.1(175)	Yebes 40m	This work
	² Π _{3/2} J = 29/2 – 27/2 a	40198.323	119.3(149)	Yebes 40m	This work
	² Π _{3/2} J = 29/2 – 27/2 b	40204.157	118.6(147)	Yebes 40m	This work
	² Π _{3/2} J = 31/2 – 29/2 a	42970.432	93.4(106)	Yebes 40m	This work
	² Π _{3/2} J = 31/2 – 29/2 b	42977.089	93.3(106)	Yebes 40m	This work
	² Π _{3/2} J = 33/2 – 31/2 a	45742.519	73.0(98)	Yebes 40m	This work
	² Π _{3/2} J = 33/2 – 31/2 b	45750.052	73.4(99)	Yebes 40m	This work
	² Π _{3/2} J = 35/2 – 33/2 a	48514.584	52.6(73)	Yebes 40m	This work
² Π _{3/2} J = 35/2 – 33/2 b	48523.044	52.2(70)	Yebes 40m	This work	
C ₄ H	N = 2 – 1 J = 3/2 – 1/2	19054.476	411.3(418) ^b	GBT	Cordiner et al. (2013)
	N = 4 – 3 J = 9/2 – 7/2	38049.654	1369(138)	Yebes 40m	This work
	N = 4 – 3 J = 7/2 – 5/2	38088.461	1007(102)	Yebes 40m	This work
	N = 5 – 4 J = 11/2 – 9/2	47566.792	1094(111)	Yebes 40m	This work
	N = 5 – 4 J = 9/2 – 7/2	47605.496	864(87)	Yebes 40m	This work
	N = 9 – 8 J = 19/2 – 17/2	85634.010	417(53)	IRAM 30m	Agúndez et al. (2008)
	N = 9 – 8 J = 17/2 – 15/2	85672.580	386(49)	IRAM 30m	Agúndez et al. (2008)
	N = 10 – 9 J = 21/2 – 19/2	95150.393	251(26)	IRAM 30m	This work
	N = 10 – 9 J = 19/2 – 17/2	95188.947	243(26)	IRAM 30m	This work
	N = 11 – 10 J = 23/2 – 21/2	104666.568	111(12)	IRAM 30m	This work
	N = 11 – 10 J = 21/2 – 19/2	104705.108	105(13)	IRAM 30m	This work
	N = 12 – 11 J = 25/2 – 23/2	114182.523	60(8)	IRAM 30m	This work
	N = 12 – 11 J = 23/2 – 21/2	114221.023	47(6)	IRAM 30m	This work
C ₈ H	² Π _{3/2} J = 53/2 – 51/2 a	31093.035	6.0(7)	Yebes 40m	This work
	² Π _{3/2} J = 53/2 – 51/2 b	31093.415	4.4(6)	Yebes 40m	This work
	² Π _{3/2} J = 55/2 – 53/2 a	32266.325	4.3(6)	Yebes 40m	This work
	² Π _{3/2} J = 55/2 – 53/2 b	32266.735	4.2(6)	Yebes 40m	This work
	² Π _{3/2} J = 57/2 – 55/2 a	33439.612	3.5(5)	Yebes 40m	This work
	² Π _{3/2} J = 57/2 – 55/2 b	33440.052	3.4(6)	Yebes 40m	This work
	² Π _{3/2} J = 59/2 – 57/2 a	34613.367	2.7(3)	Yebes 40m	This work
	² Π _{3/2} J = 59/2 – 57/2 b	34613.367	2.7(3)	Yebes 40m	This work
	² Π _{3/2} J = 61/2 – 59/2 a	35786.176	3.0(4)	Yebes 40m	This work
	² Π _{3/2} J = 61/2 – 59/2 b	35786.679	2.4(3)	Yebes 40m	This work
	² Π _{3/2} J = 63/2 – 61/2 a	36959.452	2.3(3)	Yebes 40m	This work
	² Π _{3/2} J = 63/2 – 61/2 b	36959.989	2.2(3)	Yebes 40m	This work
	² Π _{3/2} J = 65/2 – 63/2 a	38132.725	1.7(2)	Yebes 40m	This work
	² Π _{3/2} J = 65/2 – 63/2 b	38133.297	1.5(2)	Yebes 40m	This work
	² Π _{3/2} J = 67/2 – 65/2 a	39305.995	1.4(2)	Yebes 40m	This work
	² Π _{3/2} J = 67/2 – 65/2 b	39306.602	1.4(2)	Yebes 40m	This work
	² Π _{3/2} J = 69/2 – 67/2 a	40479.260	1.2(2)	Yebes 40m	This work
	² Π _{3/2} J = 69/2 – 67/2 b	40479.904	1.2(2)	Yebes 40m	This work
	² Π _{3/2} J = 71/2 – 69/2 a	41652.522	0.8(1)	Yebes 40m	This work
	² Π _{3/2} J = 71/2 – 69/2 b	41653.203	0.9(1)	Yebes 40m	This work
² Π _{3/2} J = 73/2 – 71/2 a	42825.779	0.7(1)	Yebes 40m	This work	
² Π _{3/2} J = 73/2 – 71/2 b	42826.499	0.7(1)	Yebes 40m	This work	
C ₃ N	N = 4 – 3 J = 9/2 – 7/2	39571.347	332(34)	Yebes 40m	This work
	N = 4 – 3 J = 7/2 – 5/2	39590.181	240(25)	Yebes 40m	This work
	N = 5 – 4 J = 11/2 – 9/2	49466.421	244(25)	Yebes 40m	This work
	N = 5 – 4 J = 9/2 – 7/2	49485.224	198(20)	Yebes 40m	This work
	N = 9 – 8 J = 19/2 – 17/2	89045.583	64.2(73)	IRAM 30m	This work
	N = 9 – 8 J = 17/2 – 15/2	89064.347	58.6(68)	IRAM 30m	This work
	N = 10 – 9 J = 21/2 – 19/2	98940.087	28.1(36)	IRAM 30m	This work
	N = 10 – 9 J = 19/2 – 17/2	98958.770	22.7(30)	IRAM 30m	This work
	N = 11 – 10 J = 23/2 – 21/2	108834.254	11.6(24)	IRAM 30m	This work
	N = 11 – 10 J = 21/2 – 19/2	108853.012	21.2(35)	IRAM 30m	This work
C ₅ N	N = 12 – 11 J = 25/2 – 23/2	33668.234	5.6(7)	Yebes 40m	This work
	N = 12 – 11 J = 23/2 – 21/2	33678.966	5.9(7)	Yebes 40m	This work

Table A.2. continued.

Species	Transition	Frequency (MHz)	$\int T_A^* dv$ (mK km s ⁻¹) ^a	Telescope	Reference	
	$N = 13 - 12 J = 27/2 - 25/2$	36474.308	5.8(7)	Yebes 40m	This work	
	$N = 13 - 12 J = 25/2 - 23/2$	36485.042	5.5(7)	Yebes 40m	This work	
	$N = 14 - 13 J = 29/2 - 27/2$	39280.369	5.1(7)	Yebes 40m	This work	
	$N = 14 - 13 J = 27/2 - 25/2$	39291.105	5.0(7)	Yebes 40m	This work	
	$N = 15 - 14 J = 31/2 - 29/2$	42086.415	4.7(6)	Yebes 40m	This work	
	$N = 15 - 14 J = 29/2 - 27/2$	42097.151	4.4(6)	Yebes 40m	This work	
	$N = 16 - 15 J = 33/2 - 31/2$	44892.444	4.6(6)	Yebes 40m	This work	
	$N = 16 - 15 J = 31/2 - 29/2$	44903.182	4.4(6)	Yebes 40m	This work	
	$N = 17 - 16 J = 35/2 - 33/2$	47698.457	3.7(5)	Yebes 40m	This work	
	$N = 17 - 16 J = 33/2 - 31/2$	47709.196	3.4(5)	Yebes 40m	This work	
Lupus-1A						
C ₆ H	² Π _{3/2} $J = 15/2 - 13/2 a$	20792.907	114(14) ^b	GBT	Sakai et al. (2010)	
	² Π _{3/2} $J = 15/2 - 13/2 b$	20794.475	131(16) ^b	GBT	Sakai et al. (2010)	
	² Π _{3/2} $J = 23/2 - 21/2 a$	31881.860	150.3(166)	Yebes 40m	This work	
	² Π _{3/2} $J = 23/2 - 21/2 b$	31885.541	153.1(163)	Yebes 40m	This work	
	² Π _{3/2} $J = 25/2 - 23/2 a$	34654.037	151.6(161)	Yebes 40m	This work	
	² Π _{3/2} $J = 25/2 - 23/2 b$	34658.383	150.0(159)	Yebes 40m	This work	
	² Π _{3/2} $J = 27/2 - 25/2 a$	37426.192	140.3(143)	Yebes 40m	This work	
	² Π _{3/2} $J = 27/2 - 25/2 b$	37431.255	141.0(148)	Yebes 40m	This work	
	² Π _{3/2} $J = 29/2 - 27/2 a$	40198.323	126.2(134)	Yebes 40m	This work	
	² Π _{3/2} $J = 29/2 - 27/2 b$	40204.157	124.8(130)	Yebes 40m	This work	
	² Π _{3/2} $J = 31/2 - 29/2 a$	42970.432	115.5(123)	Yebes 40m	This work	
	² Π _{3/2} $J = 31/2 - 29/2 b$	42977.089	114.9(123)	Yebes 40m	This work	
	² Π _{3/2} $J = 33/2 - 31/2 a$	45742.519	90.7(125)	Yebes 40m	This work	
	² Π _{3/2} $J = 33/2 - 31/2 b$	45750.052	91.3(128)	Yebes 40m	This work	
C ₄ H	² Π _{3/2} $J = 35/2 - 33/2 a$	48514.584	73.6(109)	Yebes 40m	This work	
	² Π _{3/2} $J = 35/2 - 33/2 b$	48523.044	66.9(103)	Yebes 40m	This work	
	$N = 4 - 3 J = 9/2 - 7/2$	38049.654	1219(123)	Yebes 40m	This work	
	$N = 4 - 3 J = 7/2 - 5/2$	38088.461	921(94)	Yebes 40m	This work	
	$N = 5 - 4 J = 11/2 - 9/2$	47566.792	1123(114)	Yebes 40m	This work	
	$N = 5 - 4 J = 9/2 - 7/2$	47605.496	846(86)	Yebes 40m	This work	
	$N = 8 - 7 J = 17/2 - 15/2$	76117.439	1124(114)	IRAM 30m	This work	
	$N = 8 - 7 J = 15/2 - 13/2$	76156.028	1024(104)	IRAM 30m	This work	
	$N = 9 - 8 J = 19/2 - 17/2$	85634.010	779(83)	IRAM 30m	This work	
	$N = 9 - 8 J = 17/2 - 15/2$	85672.580	730(77)	IRAM 30m	This work	
	$N = 11 - 10 J = 23/2 - 21/2$	104666.568	349(39)	IRAM 30m	This work	
	$N = 11 - 10 J = 21/2 - 19/2$	104705.108	334(38)	IRAM 30m	This work	
	C ₈ H	² Π _{3/2} $J = 33/2 - 31/2 a$	19359.975	10(2) ^b	GBT	Sakai et al. (2010)
		² Π _{3/2} $J = 33/2 - 31/2 b$	19360.123	9(2) ^b	GBT	Sakai et al. (2010)
C ₃ N	$N = 4 - 3 J = 9/2 - 7/2$	39571.347	251(30)	Yebes 40m	This work	
	$N = 4 - 3 J = 7/2 - 5/2$	39590.181	175(19)	Yebes 40m	This work	
	$N = 5 - 4 J = 11/2 - 9/2$	49466.421	177(19)	Yebes 40m	This work	
	$N = 5 - 4 J = 9/2 - 7/2$	49485.224	138(15)	Yebes 40m	This work	
	$N = 9 - 8 J = 19/2 - 17/2$	89045.583	141.5(150)	IRAM 30m	This work	
	$N = 9 - 8 J = 17/2 - 15/2$	89064.347	126.7(136)	IRAM 30m	This work	
	$N = 10 - 9 J = 21/2 - 19/2$	98940.087	74.6(83)	IRAM 30m	This work	
	$N = 10 - 9 J = 19/2 - 17/2$	98958.770	66.0(74)	IRAM 30m	This work	
C ₅ N	$N = 12 - 11 J = 25/2 - 23/2$	33668.234	4.5(12)	Yebes 40m	This work	
	$N = 12 - 11 J = 23/2 - 21/2$	33678.966	7.0(14)	Yebes 40m	This work	
	$N = 13 - 12 J = 27/2 - 25/2$	36474.308	4.8(11)	Yebes 40m	This work	
	$N = 13 - 12 J = 25/2 - 23/2$	36485.042	5.7(11)	Yebes 40m	This work	
	$N = 14 - 13 J = 29/2 - 27/2$	39280.369	7.8(24)	Yebes 40m	This work	
	$N = 14 - 13 J = 27/2 - 25/2$	39291.105	5.7(15)	Yebes 40m	This work	
	$N = 15 - 14 J = 31/2 - 29/2$	42086.415	4.1(9)	Yebes 40m	This work	
	$N = 15 - 14 J = 29/2 - 27/2$	42097.151	4.8(11)	Yebes 40m	This work	
	$N = 16 - 15 J = 33/2 - 31/2$	44892.444	3.2(9)	Yebes 40m	This work	
	$N = 16 - 15 J = 31/2 - 29/2$	44903.182	1.8(8) ^d	Yebes 40m	This work	
	L1527					
C ₆ H	² Π _{3/2} $J = 15/2 - 13/2 a$	20792.907	24(5) ^b	GBT	Sakai et al. (2007)	
	² Π _{3/2} $J = 15/2 - 13/2 b$	20794.475	21(5) ^b	GBT	Sakai et al. (2007)	
	² Π _{3/2} $J = 23/2 - 21/2 a$	31881.860	34.8(75)	Yebes 40m	This work	
	² Π _{3/2} $J = 23/2 - 21/2 b$	31885.541	26.0(59)	Yebes 40m	This work	
	² Π _{3/2} $J = 25/2 - 23/2 a$	34654.037	29.3(34)	Yebes 40m	This work	
	² Π _{3/2} $J = 25/2 - 23/2 b$	34658.383	31.8(37)	Yebes 40m	This work	
	² Π _{3/2} $J = 27/2 - 25/2 a$	37426.192	31.7(46)	Yebes 40m	This work	

Table A.2. continued.

Species	Transition	Frequency (MHz)	$\int T_A^* dv$ (mK km s ⁻¹) ^a	Telescope	Reference
	² Π _{3/2} $J = 27/2 - 25/2 b$	37431.255	32.2(51)	Yebes 40m	This work
	² Π _{3/2} $J = 29/2 - 27/2 a$	40198.323	32.7(50)	Yebes 40m	This work
	² Π _{3/2} $J = 29/2 - 27/2 b$	40204.157	32.3(48)	Yebes 40m	This work
	² Π _{3/2} $J = 31/2 - 29/2 a$	42970.432	30.2(47)	Yebes 40m	This work
	² Π _{3/2} $J = 31/2 - 29/2 b$	42977.089	31.1(49)	Yebes 40m	This work
	² Π _{3/2} $J = 33/2 - 31/2 a$	45742.519	30.5(48)	Yebes 40m	This work
	² Π _{3/2} $J = 33/2 - 31/2 b$	45750.052	31.3(49)	Yebes 40m	This work
	² Π _{3/2} $J = 35/2 - 33/2 a$	48514.584	27.3(48)	Yebes 40m	This work
	² Π _{3/2} $J = 35/2 - 33/2 b$	48523.044	26.9(47)	Yebes 40m	This work
C ₄ H	$N = 4 - 3 J = 9/2 - 7/2$	38049.654	388(39)	Yebes 40m	This work
	$N = 4 - 3 J = 7/2 - 5/2$	38088.461	295(30)	Yebes 40m	This work
	$N = 5 - 4 J = 11/2 - 9/2$	47566.792	434(44)	Yebes 40m	This work
	$N = 5 - 4 J = 9/2 - 7/2$	47605.496	347(35)	Yebes 40m	This work
	$N = 9 - 8 J = 19/2 - 17/2$	85634.010	747(86)	IRAM 30m	Agúndez et al. (2008)
	$N = 9 - 8 J = 17/2 - 15/2$	85672.580	712(82)	IRAM 30m	Agúndez et al. (2008)
	$N = 11 - 10 J = 23/2 - 21/2$	104666.568	542(64)	IRAM 30m	Agúndez et al. (2008)
	$N = 11 - 10 J = 21/2 - 19/2$	104705.108	487(59)	IRAM 30m	Agúndez et al. (2008)
	$N = 12 - 11 J = 25/2 - 23/2$	114182.523	462(59)	IRAM 30m	Agúndez et al. (2008)
$N = 12 - 11 J = 23/2 - 21/2$	114221.023	406(53)	IRAM 30m	Agúndez et al. (2008)	
L483					
C ₆ H	² Π _{3/2} $J = 23/2 - 21/2 a$	31881.860	29.4(34)	Yebes 40m	This work
	² Π _{3/2} $J = 23/2 - 21/2 b$	31885.541	31.0(36)	Yebes 40m	This work
	² Π _{3/2} $J = 25/2 - 23/2 a$	34654.037	28.4(32)	Yebes 40m	This work
	² Π _{3/2} $J = 25/2 - 23/2 b$	34658.383	27.7(31)	Yebes 40m	This work
	² Π _{3/2} $J = 27/2 - 25/2 a$	37426.192	26.2(29)	Yebes 40m	This work
	² Π _{3/2} $J = 27/2 - 25/2 b$	37431.255	26.2(30)	Yebes 40m	This work
	² Π _{3/2} $J = 29/2 - 27/2 a$	40198.323	24.4(28)	Yebes 40m	This work
	² Π _{3/2} $J = 29/2 - 27/2 b$	40204.157	23.2(27)	Yebes 40m	This work
	² Π _{3/2} $J = 31/2 - 29/2 a$	42970.432	19.7(23)	Yebes 40m	This work
	² Π _{3/2} $J = 31/2 - 29/2 b$	42977.089	20.4(24)	Yebes 40m	This work
	² Π _{3/2} $J = 33/2 - 31/2 a$	45742.519	13.6(22)	Yebes 40m	This work
	² Π _{3/2} $J = 33/2 - 31/2 b$	45750.052	14.2(21)	Yebes 40m	This work
C ₄ H	² Π _{3/2} $J = 35/2 - 33/2 a$	48514.584	13.0(23)	Yebes 40m	This work
	² Π _{3/2} $J = 35/2 - 33/2 b$	48523.044	13.7(24)	Yebes 40m	This work
	$N = 4 - 3 J = 9/2 - 7/2$	38049.654	470(48)	Yebes 40m	This work
	$N = 4 - 3 J = 7/2 - 5/2$	38088.461	356(36)	Yebes 40m	This work
	$N = 5 - 4 J = 11/2 - 9/2$	47566.792	439(50)	Yebes 40m	This work
	$N = 5 - 4 J = 9/2 - 7/2$	47605.496	352(36)	Yebes 40m	This work
	$N = 8 - 7 J = 17/2 - 15/2$	76117.439	375(38)	IRAM 30m	This work
	$N = 8 - 7 J = 15/2 - 13/2$	76156.028	337(35)	IRAM 30m	This work
	$N = 9 - 8 J = 19/2 - 17/2$	85634.010	272(27)	IRAM 30m	Agúndez et al. (2019)
	$N = 9 - 8 J = 17/2 - 15/2$	85672.580	249(24)	IRAM 30m	Agúndez et al. (2019)
	$N = 10 - 9 J = 21/2 - 19/2$	95150.393	157(15)	IRAM 30m	Agúndez et al. (2019)
	$N = 10 - 9 J = 19/2 - 17/2$	95188.947	147(14)	IRAM 30m	Agúndez et al. (2019)
$N = 11 - 10 J = 23/2 - 21/2$	104666.568	110(10)	IRAM 30m	Agúndez et al. (2019)	
$N = 11 - 10 J = 21/2 - 19/2$	104705.108	100(9)	IRAM 30m	Agúndez et al. (2019)	
$N = 12 - 11 J = 25/2 - 23/2$	114182.523	64(6)	IRAM 30m	Agúndez et al. (2019)	
$N = 12 - 11 J = 23/2 - 21/2$	114221.023	64(6)	IRAM 30m	Agúndez et al. (2019)	
L1495B					
C ₆ H	² Π _{3/2} $J = 13/2 - 11/2 a$	18020.606	55(10) ^c	GBT	Gupta et al. (2009)
	² Π _{3/2} $J = 13/2 - 11/2 b$	18021.783	55(10) ^c	GBT	Gupta et al. (2009)
	² Π _{3/2} $J = 21/2 - 19/2 a$	29109.658	141.6(164) ^b	GBT	Cordiner et al. (2013)
	² Π _{3/2} $J = 23/2 - 21/2 a$	31881.860	51.9(59)	Yebes 40m	This work
	² Π _{3/2} $J = 23/2 - 21/2 b$	31885.541	47.9(53)	Yebes 40m	This work
	² Π _{3/2} $J = 25/2 - 23/2 a$	34654.037	46.8(52)	Yebes 40m	This work
	² Π _{3/2} $J = 27/2 - 25/2 a$	37426.192	45.4(51)	Yebes 40m	This work
	² Π _{3/2} $J = 27/2 - 25/2 b$	37431.255	42.8(49)	Yebes 40m	This work
	² Π _{3/2} $J = 29/2 - 27/2 a$	40198.323	36.2(42)	Yebes 40m	This work
	² Π _{3/2} $J = 29/2 - 27/2 b$	40204.157	37.7(42)	Yebes 40m	This work
	² Π _{3/2} $J = 31/2 - 29/2 a$	42970.432	33.3(40)	Yebes 40m	This work
	² Π _{3/2} $J = 31/2 - 29/2 b$	42977.089	33.6(40)	Yebes 40m	This work
	² Π _{3/2} $J = 33/2 - 31/2 a$	45742.519	24.7(38)	Yebes 40m	This work
	² Π _{3/2} $J = 33/2 - 31/2 b$	45750.052	24.0(35)	Yebes 40m	This work
	² Π _{3/2} $J = 35/2 - 33/2 a$	48514.584	19.4(32)	Yebes 40m	This work

Table A.2. continued.

Species	Transition	Frequency (MHz)	$\int T_A^* dv$ (mK km s ⁻¹) ^a	Telescope	Reference
	² Π _{3/2} $J = 35/2 - 33/2$ b	48523.044	18.6(33)	Yebes 40m	This work
L1544					
C ₆ H	² Π _{3/2} $J = 13/2 - 11/2$ a	18020.606	51(11)	GBT	Gupta et al. (2009)
	² Π _{3/2} $J = 13/2 - 11/2$ b	18021.783	50(11)	GBT	Gupta et al. (2009)
	² Π _{3/2} $J = 23/2 - 21/2$ a	31881.860	23.8(36)	Yebes 40m	This work
	² Π _{3/2} $J = 23/2 - 21/2$ b	31885.541	30.0(44)	Yebes 40m	This work
	² Π _{3/2} $J = 25/2 - 23/2$ a	34654.037	25.7(39)	Yebes 40m	This work
	² Π _{3/2} $J = 25/2 - 23/2$ b	34658.383	31.6(48)	Yebes 40m	This work
	² Π _{3/2} $J = 27/2 - 25/2$ a	37426.192	23.3(36)	Yebes 40m	This work
	² Π _{3/2} $J = 27/2 - 25/2$ b	37431.255	19.9(34)	Yebes 40m	This work
	² Π _{3/2} $J = 29/2 - 27/2$ b	40204.157	18.0(31)	Yebes 40m	This work
	² Π _{3/2} $J = 31/2 - 29/2$ a	42970.432	13.6(26)	Yebes 40m	This work
	² Π _{3/2} $J = 31/2 - 29/2$ b	42977.089	12.1(23)	Yebes 40m	This work
L1521F					
C ₆ H	² Π _{3/2} $J = 13/2 - 11/2$ a	18020.606	36(10)	GBT	Gupta et al. (2009)
	² Π _{3/2} $J = 13/2 - 11/2$ b	18021.783	26(9)	GBT	Gupta et al. (2009)
L1251A					
C ₆ H	² Π _{3/2} $J = 21/2 - 19/2$ a	29109.658	36(8)	GBT	Cordiner et al. (2011)
	² Π _{3/2} $J = 21/2 - 19/2$ b	29112.730	35(8)	GBT	Cordiner et al. (2011)
	² Π _{3/2} $J = 21/2 - 19/2$ a	29109.658	43.6(65) ^b	GBT	Cordiner et al. (2013)
L1512					
C ₆ H	² Π _{3/2} $J = 13/2 - 11/2$ a	18020.606	20(7) ^c	GBT	Gupta et al. (2009)
	² Π _{3/2} $J = 13/2 - 11/2$ b	18021.783	20(7) ^c	GBT	Gupta et al. (2009)
	² Π _{3/2} $J = 21/2 - 19/2$ a	29109.658	27(5)	GBT	Cordiner et al. (2011)
	² Π _{3/2} $J = 21/2 - 19/2$ b	29112.730	28(5)	GBT	Cordiner et al. (2011)
	² Π _{3/2} $J = 21/2 - 19/2$ a	29109.658	26.3(35) ^b	GBT	Cordiner et al. (2013)
L1172					
C ₆ H	² Π _{3/2} $J = 21/2 - 19/2$ a	29109.658	41.1(57) ^b	GBT	Cordiner et al. (2013)
L1389					
C ₆ H	² Π _{3/2} $J = 13/2 - 11/2$ a	18020.606	10(6) ^c	GBT	Gupta et al. (2009)
	² Π _{3/2} $J = 13/2 - 11/2$ b	18021.783	10(6) ^c	GBT	Gupta et al. (2009)
	² Π _{3/2} $J = 21/2 - 19/2$ a	29109.658	27.1(40) ^b	GBT	Cordiner et al. (2013)
TMC-1 C					
C ₆ H	² Π _{3/2} $J = 21/2 - 19/2$ a	29109.658	88.1(105) ^b	GBT	Cordiner et al. (2013)

^a Unless otherwise stated, the intensity scale is antenna temperature (T_A^*). It can be converted to main beam brightness temperature (T_{mb}) by dividing by B_{eff}/F_{eff} (see caption of Table A.1). The error in $\int T_A^* dv$ includes the contributions from the Gaussian fit and from calibration (assumed to be 10%). ^b Intensity scale is T_{mb} . ^c Intensity distributed equally among the two fine components. ^d Marginal detection.